Chapter 14

Geomathematics

Chapter outline

Geologic Time Scale 2020. DOI: https://doi.org/10.1016/B978-0-12-824360-2.00014-0

SubChapter 14A

Geomathematical and Statistical Procedures

F.P. Agterberg, A-C. Da Silva and F.M. Gradstein

Abstract

The input for the calculation of a numerical time scale is a set of radioisotopic dates with variable uncertainty in both time (in Myr) and stratigraphic position (in biozones). These selected input dates are irregularly distributed with respect to a biostratigraphic scale derived from graphical correlation, constrained optimization, or a stack of successive biozonal units. Spline fitting with error estimation produces a linear time scale with error bars on the geologic stage boundary ages. These methods were applied to data sets developed for the Ordovician–Silurian, Devonian, and Carboniferous–Permian periods. Detailed Early and Late Cretaceous data sets were both splined and results adjusted from comparative summations and adjusting of cyclostratigraphic and M-sequence splining durations.

14A.1 History

Geologic time scales (GTS) are constructed by combining stratigraphic information with radioisotopic dates and their standard deviations. The stratigraphic record to be used includes litho-, bio-, chrono-, cyclo-, and magnetostratigraphy. For the construction of several previous time scales, ages of stage boundaries were estimated by application of the chronogram method (Harland et al., 1982, 1990), or maximum likelihood (Gradstein et al., 1994, 1995), to a worldwide database of chronostratigraphically classified dates. These methods, which can also be applied to more closely spaced zone boundaries (Pálfy et al., 2000), resulted in age estimates accompanied by approximate 95% confidence intervals. A final time scale was obtained by calibration using graphical and curve-fitting methods, including cubic smoothing splines.

Odin (1994) discussed three separate approaches to numerical time scale construction: statistical, geochronological, and graphical methods, but in the end preferred subjective reasoning to estimate ages of samples and stratigraphic boundaries. Gradstein et al. (1994, 1995) used all three approaches in a stepwise procedure involving maximum likelihood, use of stratigraphically constrained dates, and recalibration by curve fitting.

14A.1.1 The chronogram method

The chronogram method used by Harland et al. (1982, 1990) is suitable for the estimation of the age of chronostratigraphic boundaries from a radioisotopic database when most rock samples used for age determination are subject to significant relative uncertainty. Inconsistencies in the vicinity of chronostratigraphic boundaries can then be ascribed to imprecision of the age determination method.

Cox and Dalrymple (1967) originally developed an approach for estimating the age of Cenozoic chron boundaries from inconsistent K–Ar age determinations of basaltic rocks. Harland et al. (1982, 1990) adopted this method in their calculations of ages of stage boundaries for the 1982 and 1990 time scales. The basic principle of this approach is as follows: assuming a hypothetical trial age for an observed chronostratigraphic boundary, rock samples from above this boundary should be younger, and those below it should be older. An inconsistent date is either an older date for a rock sample known to be younger than the trial date or a younger date for a sample known to be older. The difference between each inconsistent date and the trial age can be standardized by dividing it by the standard deviation of the inconsistent date. Thus relatively imprecise dates receive less weight than more precise dates. The underlying assumptions are that (1) the rock samples are uniformly distributed along the time axis and (2) the error of each date satisfies a normal (Gaussian) error distribution with standard deviation equal to that of the age determination method used.

Standardized differences between inconsistent dates and trial age can be squared and the sum of squares (written as E^2) determined for all inconsistent dates corresponding to the same trial age. Chronograms constructed by Harland et al. (1982) were U-shaped plots of E^2 against different trial ages spaced at narrow time intervals. The optimum choice of age was at the trial age where E^2 was a minimum.

Agterberg (1988) made the following improvement to this method. In addition to inconsistent dates, there are generally more consistent dates for any trial age selected for a chronostratigraphic boundary. The statistical maximum likelihood method can be used to combine consistent with inconsistent dates resulting in an improved estimate of the age of the chronostratigraphic boundary considered. Each standardized difference with respect to a trial age was interpreted as the fractile of the normal distribution in standard form and transformed into its corresponding probability. Summation of the logarithmically transformed probabilities then yields the log-likelihood value of the trial date. In this type of calculation, inconsistent dates receive more weight than consistent dates. Consequently, the improvement resulting from using consistent dates, in addition to the inconsistent dates, is relatively minor. However, when there are relatively few dates, use of the consistent dates yields significantly better results. The log-likelihood function is beehive-shaped. For example, see Gradstein et al. (1995).

A general disadvantage of chronogram methods is that the relative stratigraphic position of the sample is

generalized with respect to stage boundaries that are relatively far apart in time. The relative stratigraphic position of one sample with respect to another within the same stage is not considered. A better approach is to incorporate relative stratigraphic positions of fewer samples for which precise age determinations are available.

14A.1.2 The McKerrow method

McKerrow et al. (1985) described the following type of method to construct a numerical time scale for the Ordovician, Silurian, and Devonian. Use was made of an iterative construction involving a sequence of diagrams wherein the isotopic age of the sample was plotted along the x-axis and its stratigraphic age along the y-axis. They stated (p. 73),

> *Most graphs are constructed with definite numerical scales along both the x and y axes; this is not the case with fig. 1, where only the horizontal (x) axis is numerical. The vertical (y) axis is a stratigraphic time scale, showing periods, series, stages and zones; the precise duration of each of these time divisions is unknown. In fact, the whole object of this documentation is to determine, as far as possible with the evidence available, what estimates can be given on the duration of these stratigraphic divisions. Thus, in the course of preparing this figure, we have constructed a series of graphs, each with slightly differing vertical scales, until we obtained a scale which allowed a straight line to pass through almost all the rectangles representing the analytical errors (2σ) and the stratigraphic uncertainties in the data we use.*

In a later paper on the Ordovician time scale, Cooper (1999) used 14 analytically reliable and stratigraphically controlled high-resolution TIMS U–Pb zircon dates and a single Sm–Nd date. Adopting a modified version of the McKerrow method, Cooper plotted these Ordovician dates along a relative time scale that was then reproportioned as necessary to achieve a good fit with a straight line obtained by linear regression. This method of relative shortening and lengthening of parts of the Ordovician time scale was based mainly on a comparison of sediment accumulation rates in widely different regions and, to some extent, on empirical reproportioning. Agterberg (2002) subjected Cooper's (1999) data to spline fitting and found that the optimum smoothing factor (SF) corresponds to a straight-line fit. He then used Ripley's MLFR (Maximum Likelihood for Functional Relationship, Ripley and Thompson, 1987) method to fit a straight line in which stratigraphic uncertainty was considered as well.

14A.2 Spline fitting in GTS2004

The approach adopted by GTS2004 placed more emphasis on the relative stratigraphic position of the few samples for which precise age dates were available. It was based on methods of straight-line construction applied to more or less homogeneous data sets previously developed for Paleozoic periods. The starting point for construction of numerical time scales is a data set of radioisotopic ages, measured in millions of years, with 2-sigma error bars, for samples positioned along a relative stratigraphic scale of which the unit is approximately proportional to time (also measured in millions of years). In GTS2004, spline-curve fitting was used to relate the observed ages to their stratigraphic position. GTS2012 used the same method except for a new approach to the estimation of error bars on zonal boundaries.

The first stage consists of fitting a cubic smoothing spline curve according to the method previously described in detail for the Mesozoic time scale in Gradstein et al. (1994, 1995) and Agterberg (1988, 1994). As shown in the example in Fig. 14A.1 age determinations are plotted in the vertical direction (along the y-axis) against relative stratigraphic position (x-axis). Relative stratigraphic position is according to a continuous scale that is the same for all age determinations used. To some extent, the scale initially used for relative stratigraphic position determines the shape of the final spline curve. A relative stratigraphic scale should be used that is as close as possible to the numerical GTS (in millions of years) except for a linear transformation. Less satisfactory relative stratigraphic scales used in the past included scales based on sediment accumulation corrected for differences in rates of sedimentation, the hypothesis of equal duration of stages (Harland et al., 1982), and the hypothesis of equal duration of biozones (Kent and Gradstein, 1986; Harland et al., 1990; Gradstein et al., 1995).

14A.2.1 Incorporation of stratigraphic uncertainty

Each age determination is weighted according to the inverse of its variance corresponding to the published 2-sigma (or 1-sigma) error bar. If stratigraphic uncertainty is incorporated, this variance becomes $s_t^2(y) = s^2(x) + s^2(y)$ instead of $s^2(y)$. The rationale behind this relatively simple transformation is that the x-axis also represents a time scale. Uncertainty in relative stratigraphic position should also be reflected in uncertainty of the location of a date in the x–y plot. In Paleozoic applications the stratigraphic error bars can be relatively large. Stratigraphic uncertainty then adds to the uncertainty expressed by the 2-sigma error bars of the age determinations. A rectangular frequency distribution model represents stratigraphic uncertainty better than the Gaussian frequency distribution model employed for the measurement errors of the dates. The underlying assumption is that a sample reported to occur within a particular zone, or within two or more consecutive

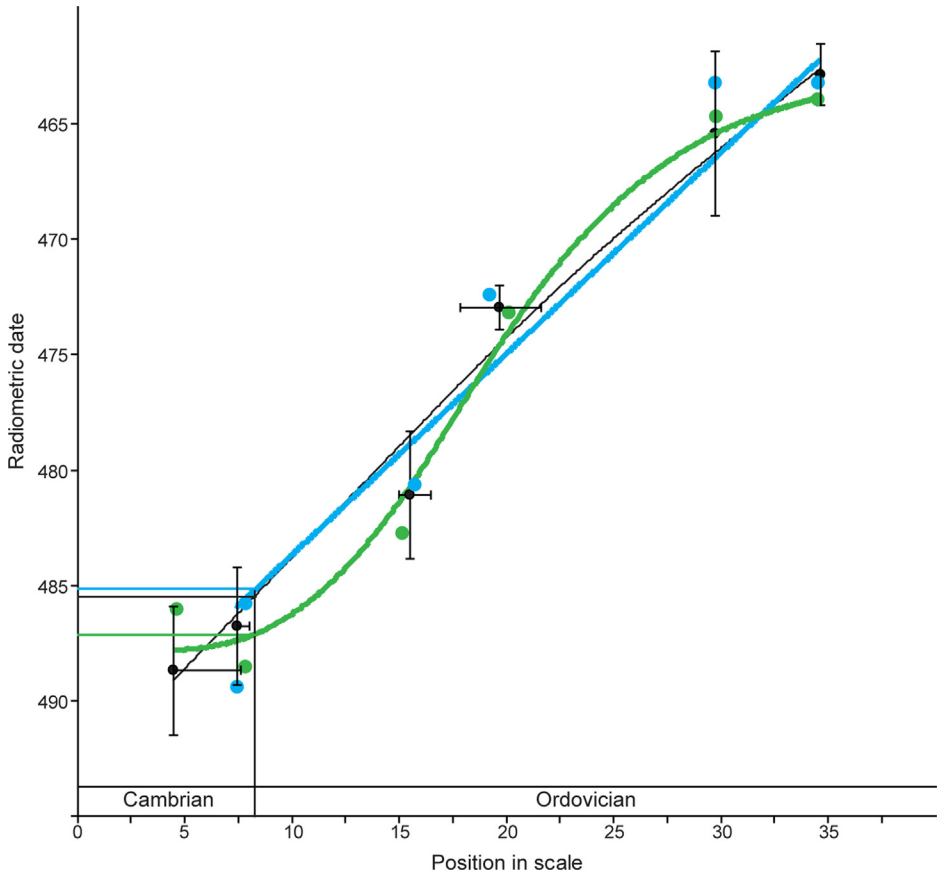

FIGURE 14A.1 Illustration of the splining procedure with a small set of data points around the Cambrian–Ordovician boundary (from GTS2012, this figure). Black dots: given data with stratigraphic and radioisotopic dating error bars (total range and 2-sigma). Black curve: spline of the given data, cross-validated SF = 1.075. Blue dots: random replicate of the input data generated according to the given points and their error bars, SF = 2.125. Blue curve: spline of the random replicate. Green dots and curve: another random replicate and its spline, SF = 0.85. The Cambrian–Ordovician boundary age from the spline of the given data is 485.39 Ma. The ages computed from the random replicates are 485.17 and 487.06 Ma. *SF*, Smoothing factor.

zones, could occur anywhere within this chronostratigraphic interval with equal probability for all places where it truly occurs. If the length of a stratigraphic error bar is written as q, the variance of a rectangular frequency density distribution (with base q) is $q^2/12$ instead of $q^2/16$ for the Gaussian distribution. This translates into a standard deviation $s(x) = 1.15q/4$ (cf. Agterberg, 2002). The stratigraphic error bars used for analysis in GTS2004 and GTS2020 were treated in this manner.

Ideally, when stratigraphic standard deviations $s(x_i)$ are to be combined with $s(y_i)$ values, x_i and y_i as well as $s(x_i)$ and $s(y_i)$ are expressed in millions of years and the line of best fit would have the simple equation $y = x$. This strategy followed for GTS2004 applications is comparable to that discussed by Press et al. (1992) for straight-line fitting with both variables subject to uncertainty. The procedure goes back to a simple method for dealing with this problem originally devised in 1984 by Lybanon (1984). In our applications the final spline curves are usually not very different from straight lines and variances along both axes become comparable when Ma is used for both scales. For $s(x_i)$ values a good approximation is obtained by setting the interval between oldest and youngest observed ages along the relative scale equal to the difference between these two ages in millions of years. However, with the increases of both quantity and quality of age determinations, deviations between best fitting spline curves and straight lines have become better established than in the past.

14A.2.2 Smoothing splines

A cubic smoothing spline $f(x)$ is fully determined by n pairs of values (x_i, y_i), the standard deviations of the dates $s(y_i)$, and an SF representing the square root of the average value of the squares of scaled residuals $r_i = (y_i - f(x_i))/s(y_i)$. In general, if all $s(y_i)$ values are unbiased, SF ≈ 1, or SF is equal to a value slightly less than 1 (cf. Agterberg, 1994). If SF significantly exceeds 1, this suggests that some or all of the variances used are too small (underreported). Thus the spline-fitting method may provide an independent method

of assessing mutual consistency and average precision of published 2-sigma error bars.

The method of "leaving-one-out" cross-validation (CV) can be used to determine the optimum SF. In this method, all observed dates y_i, between the oldest and youngest one, are successively left out from spline fitting with preselected trial values of SF. The result is $(n-2)$ spline curves for each SF tried. The CV value for any SF is the sum of squares of deviations between y_i and estimated values on the $(n-2)$ spline curves with the same x_i values as y_i. The best SF has the smallest CV value.

It is noted that even if the CV pattern shows a well-developed minimum at a value not close to 1, adoption of the optimum SF value instead of SF = 1 generally constitutes only a minor improvement of the spline curve. In Paleozoic applications (see Section 8.2, Chapter 8 in Gradstein et al., 2004), the optimum SF is generally smaller than 1. Setting SF = 1 would result in slightly more smooth-spline curves.

Unless its unit is consistently proportional to geologic time measured in millions of years, the numerical time scale resulting from spline fitting is not linearly related to the initial relative time scale. It is, however, linearly related to geologic time in millions of years. This allows for gradual changes over time in the original hypothetical process on the basis of which the initial relative time scale is constructed. For example, deviations from a straight line on a fitted spline curve may represent corrections of changes in sedimentation rate or rate of evolutionary change.

In GTS2004, distances between successive points along the x-axis in $x-y$ plots were not zero or close to zero. In the spline fitting, separate cubic polynomials are fitted between pairs of points taking care that the resulting spline curve is continuous not only in age but also in its first derivative (changes in age). If distances between successive points are either zero or negligibly small, cubic polynomials cannot be fitted. Situations of this type arise when successive ash layers, which are close to one another, are dated separately. This can result in problems in the spline fitting, especially when the leaving-one-out method is used for CV. Such problems can be avoided by calculating the weighted average of dates with approximately the same values along the stratigraphic scale, as will be discussed in Section 14A.5.1.

14A.2.3 Treatment of outliers

It often happened that a few points ended up far away from the smoothing spline curve. These outliers are handled by assuming that their standard deviations must have been underestimated. The procedure contains a step where outliers are identified and their standard deviations adjusted. The spline can then be recomputed.

Individual scaled residuals are either positive or negative and should be approximately distributed as z-values (from the "standard normal" Gaussian frequency distribution). Their squares are then chi-square distributed with one degree of freedom and can be converted into probabilities to test the hypothesis that they are not greater than can be expected on the basis of the $s(y)$ values used for scaling the residuals. The sum of squares of several scaled residuals is also approximately distributed as chi-square but with a larger number of degrees of freedom. A statistical test can therefore be used for identifying the relatively few outliers exhibiting error bars that are much narrower than expected on the basis of most ages in the same data set.

The $s(y)$ values can be revised by replacing probabilities that are too small ($P < .05$) by 0.5. Setting the probability equal to 50% is equivalent to replacing the chi-square value by 0.4549. This is the same as adopting a new z-value of 0.674, because chi-square with a single degree of freedom is z^2. The new $s(y)$ value is then computed by dividing the old z-value (scaled residual) by 0.674, and multiplying the result with the original $s(y)$.

14A.2.4 Ages of zonal boundaries

Ages of zonal boundaries, and durations of zones, are estimated by interpolating the spline curve. In GTS2004, error bars on zonal boundaries were estimated through a sequence of steps. First, the spline curve was "rectified" by plotting the original dates y_i on the x-axis and the spline values $f(x_i)$ on the y-axis. This data set was subjected to a linear regression (MLFR), giving error bars on slope and intercept. These were again used to estimate standard deviations of residuals. Finally, the latter deviations formed the basis of errors on zonal boundaries using adjustment and smoothing (ramping). This procedure assumed that the spline fitting had provided an exact adjustment for variation in slope of the chronostratigraphy versus age curve.

14A.3 Modifications in GTS2012

New stratigraphic information, including new age dates, had become available after GTS2004. This information was incorporated for GTS2012, which was an update of GTS2004. Statistical methods were not changed significantly except for a new method for the estimation of error bars on stage boundary ages. The new age estimates result mainly from the fact that new spline curves were fitted relating updated age data sets to earlier time scales. These earlier time scales were either GTS2004 or other GTS.

In GTS2004, error bars were estimated using an MLFR regression of the rectified spline. GTS2012 uses a more direct approach, but also a somewhat different definition of errors. Given our spline-fitting procedure and the inaccuracy of the estimates of radioisotopic dates and

stratigraphic positions, we may ask how much an interpolated zonal boundary date would have varied if we carried out the datings, spline fitting, and interpolation repeatedly.

14A.3.1 Bootstrap splines

This is simulated by a Monte Carlo procedure, picking random stratigraphic positions and dates with distributions as given (normal or rectangular) and then running the spline fitting anew with CV (Fig. 14A.1). This is repeated say 10,000 times, producing a histogram of interpolated values from which a 95% confidence interval can be derived. The procedure is computer intensive; for each of the 10,000 Monte Carlo replicates, a number of splines must be computed in the CV procedure. Analytical approaches for the computation of confidence intervals on smoothing splines with error bars on both axes are not available.

The analogy to actual repeated measurement is only approximate, because the replicate distributions are not centered on the actual precise radioisotopic dates, nominally corresponding to the population means of repeated measurement, but on *estimated* radioisotopic dates. It was not investigated to what extent this may influence the error bars.

14A.3.2 Monotonicity

Some replicates may have combinations of extreme random data values that produce serious wiggles in the spline curve resulting from the bootstrap method. To reduce the possibly large effects of this phenomenon on interpolated values, the SF was automatically increased from the optimum value until the curve in monotonically increasing (no time reversal).

The splining procedure rests on the assumption that absolute time is a smooth function of stratigraphic position. This is a pragmatic, parsimonious assumption, but it is easy to imagine situations where it is not true (e.g., a global hiatus). Possible violations of the smoothness assumption may increase error bars by an unknown amount.

In addition, it should be noted that the Monte Carlo procedure for generating error bars assumes that the errors in radioisotopic dates are independent. In reality, these errors are partitioned into "internal" and "external" errors. Only the internal errors are truly independent, while the external errors are highly correlated across samples. Our treatment of all errors as completely independent is expected to lead to some underestimation of the errors on interpolated boundary ages. For the estimation of error bars on *durations*, we use only the internal errors for the Monte Carlo procedure, because external errors will influence the age of the lower and upper boundaries of a stage or period by approximately the same amount and therefore will not contribute significantly to duration error. The iterative procedure involving random sampling of rectangular uncertainty boxes used in GTS2012 worked well except for the Devonian where part of the final spline curve was replaced by a straight-line segment connecting the age determinations for samples D7 in the Eifelian and D9 in the Frasnian. These two dates had relatively small 2-sigma values and no significant stratigraphic uncertainty.

Obvious problems with the GTS2012 Devonian spline are that several of the 18 original age determinations (D4, D5, D6, D9, and D15) used have 2-sigma error bars that do not intersect with the age-stratigraphic position curve in Fig. 22.14 of GTS2012. Only approximately 5% of these error bars (i.e., probably a single error bar for the Devonian) should intersect with the curve. It indicates that the method of constructing the Devonian GTS2012 spline curve was not fully satisfactory. Problems encountered when the bootstrap spline was fitted to the Devonian were already described in GTS2012 (p. 587) as follows: In the first run of the smoothing spline procedure the CV suggested an optimum SF of 1.85. With such a high SF, six of the data points did not pass the chi-square test (D4, $\chi^2 = 8.12$, $P = .004$; D5, $\chi^2 = 21.7$, $P = .000$; D6, $\chi^2 = 0.005$, $P = .020$; D8, $\chi^2 = 7.85$, $P = .005$; D9, $\chi^2 = 4.86$, $P = .032$; and D15, $\chi^2 = 4.43$, $P = .035$). For each of these points the combined stratigraphic and radioisotopic error $s_t(y)$ was therefore increased to enforce a P value of .5. The adjusted errors were used for a second computation of the spline. In this new run the optimum SF was 0.45. The resulting final spline was shown in GTS2012 Fig. 22.14A. As pointed out before, it deviates significantly from six observed dates and probably needed the straight-line segment correction for top and base of the Givetian.

14A.3.3 Multipeaked BChron confidence intervals

The GTS2012 Devonian time scale was critically evaluated by De Vleeschouwer and Parnell (2014). These authors applied the BChron *R* software package (Haslett and Parnell, 2008) to the Devonian time scale using GTS2012 dates as input (also see later in this chapter). BChron is based on a continuous Markov monotone stochastic process model originally used for combining chronological information arising from ^{14}C dates with depth data in sedimentary sections. The sedimentary process is simulated using compound Poisson-gamma density functions. The gamma function used by Haslett and Parnell (2008) has two parameters and resembles a Gaussian curve that is bounded at both ends so that the principle of monotonicity is not violated. In addition, the Poisson distribution has a single parameter.

In their application to the Devonian, De Vleeschouwer and Parnell (2014) point out that their estimates of the stage boundary ages do not differ significantly from those in GTS2012. However, the uncertainty limits of their

estimates are significantly different because they depend strongly on density of age determinations along the geologic time line. Clustering of age determinations will be discussed in more detail in the next section. Here it is noted that the BChron software used by De Vleeschouwer and Parnell (2014) requires that the input dates satisfy the principle of monotonicity in that younger dates should not be preceded by older dates in the direction of time along the stratigraphic scale. Nonoverlapping error bars are manually shifted in order to satisfy this input requirement.

When there are obvious inconsistencies of this type like the one involving D4 and D5 in Fig. 14A.2, it is not clear what should be done. Shifting one or both data points along the time axis is equivalent to assuming one or two inaccuracies. The approach taken in GTS2004 and GTS2012 was that, when inconsistencies of this type arise, precision of one or both dates was probably overestimated and error bars along the *y*-axis were made longer by using the chi-square test. In the approach that resulted in Fig. 14A.2 uncertainties were enlarged to some extent by incorporating the stratigraphic uncertainty before the spline curve was fitted.

In general, BChron results show a 95% confidence belt with relatively many points of narrowing and widening (also see Ovtcharova et al., 2015). These points tend to coincide with the locations of one or more relatively precise age determinations. De Vleeschouwer and Parnell (2014) argue that a confidence belt of this type is to be preferred to the type of confidence belt resulting from least-squares curve fitting, which tends to be narrow near the middle and widens toward the points at the beginning and end of the series of *x*-values used. The reason for these widenings of the 95% confidence belt is simply that there are no data points before and after the beginning and end of the time series. If locally there is high density of points along the *x*-axis, these points will contribute more than average to the coefficients that are being estimated by the method of least squares. It is noted that best fitting spline curves also satisfy the principle of least squares.

14A.3.4 Silver spikes

The relatively high confidence points in the BChron curve could be regarded as "silver spikes" in analogy with the golden spikes at stage boundaries where quality and quantity of information are above average. It is likely that in the immediate vicinities of the sample locations selected for age determination, quality of geological information is

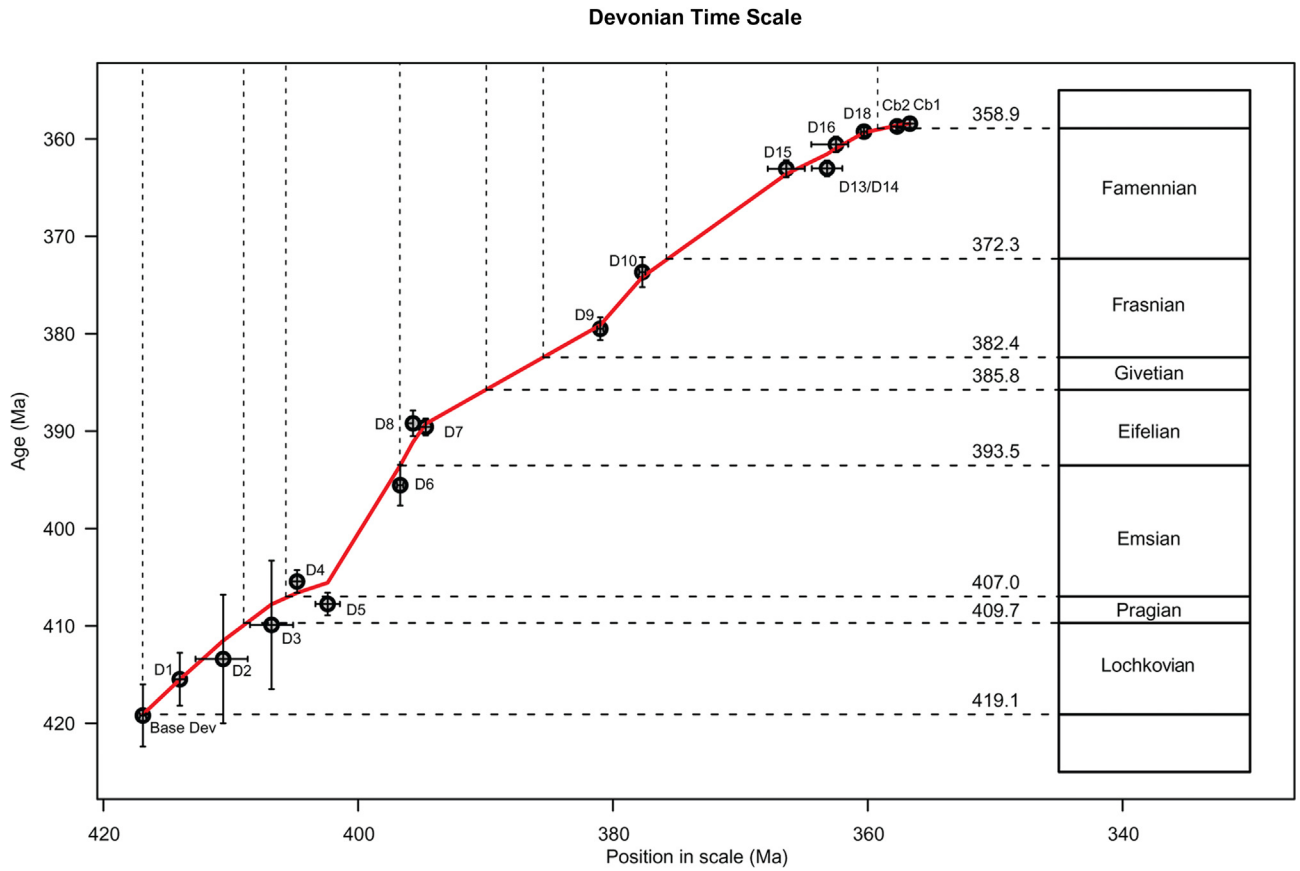

FIGURE 14A.2 Devonian time scale based on smoothing spline fitted to composite interval age determinations and stratigraphic uncertainties in GTS2012.

above average but not as good as at the golden spikes. Depending on how the silver spikes in Figures 1 and 2 of De Vleeschouwer and Parnell (2014) are counted, there would be about 10 silver spikes in the Devonian. On the other hand, statistically (see Section 14A.4), there is no conclusive evidence of significant clustering for so many silver spikes along the stratigraphic scale. In the next section the problem of clustering of ash layers with age determinations will be considered in more detail and later (Section 14A.5.5) an approximate 95% confidence belt will be constructed on the basis of the GST2020 age determinations for the Devonian.

It is noted that a technique such as LOWESS or its later version LOESS (see, e.g., Howarth and McArthur, 1997) also can produce 95% confidence belts with local maxima and minima in thickness. However, when there are relatively few data points as for the Devonian dates, no meaningful LOESS confidence belts can be computed.

14A.3.5 Revised Devonian Spline

The smoothing spline shown in Fig. 14A.2 does not show any of these drawbacks mentioned previously. It was derived using the publicly available *R*-program *smooth-spline* as implemented by B.D. Ripley and M. Maechler in *R*.Stats Package version 3.6.0, with uncertainties based on total variances $s_t^2(y)$ instead of on s^2 (y) and use of CV. This approach was also adopted for GTS2020 Paleozoic spline curves (Section 14A.5.5).

The new smoothing spline (Fig. 14A.2) closely resembles the GTS2012 Devonian spline modified by connecting the dates for samples D7 and D9 with the straight-line segment. Moreover, this new curve is intersected by the 2-sigma error bars of all input dates except two (D5 and D13/D14). The two main modifications used are that stratigraphic uncertainty was included by using total variance $s_t^2(y)$ and CV. A minor modification in the input data consisted of combining the dates for D13 and D14 into a single value according to the method to be described in Section 14A.5.1, because they have the same position in stratigraphic scale. Their weighted average has narrower 2-sigma error bar.

In comparison with other Paleozoic periods, relatively few age determinations continue to be available for the Devonian. For GTS2012 a bootstrap method was used obtaining an average spline curve based on 10,000 individual splines each based on random sampling of random variables for all dates with normal (Gaussian) distributions in the *y*-direction and rectangular distributions in the *x*-direction. As mentioned before, the Devonian also has been the subject of a study by De Vleeschouwer and Parnell (2014) who applied a different method (Bchron) for deriving the curve relating the age determinations to the stratigraphic scale. In this section special attention is paid to the Devonian, which has a notable lack of data for the Givetian and parts of its adjoining stages. It suggests that worldwide there exist gaps in the density distribution of age determinations along the stratigraphic scale. This may present a third source of uncertainty in time scale estimation that is independent of age determination errors and stratigraphic uncertainty. The original GST2012 data for the Devonian, which were also used by De Vleeschouwer and Parnell (2014), will be used in the next section to investigate the possibility of spatial clustering of Devonian ash beds used for the age determinations.

Table 14A.1 is a summary of interpolated ages of Devonian epoch and stage boundaries in:

1. GTS2012, using cubic splining and CV, with bootstrapped error bars (one-sided);
2. GTS2020 data, using *R* cubic splining, clustering analysis and CV, with the spline shown in Fig. 22.14 of Chapter 22, The Devonian Period (Becker et al., this book); and
3. GTS2012, using BChron and clustering analysis (De Vleeschouwer and Parnell, 2014).

There is no significant difference in age estimates using *R* cubic splining + or BChron +, with stage

TABLE 14A.1 Summary of interpolated ages of Devonian epoch and stage boundaries.

Base of Stage	GTS2012 Age (Ma)		GTS2020 Age (Ma)		BChron-2014 Age (Ma)	
Tournaisian	358.9	± 0.4	359.3	± 0.3	359.1	± 0.4
Famennian	372.2	± 1.6	371.4	± 0.6	372.8	1.8/ − 3.2
Frasnian	382.7	± 1.0	379	± 0.9	382.5	3.5/ − 2.6
Givetian	387.7	± 0.8	385.9	± 1.5	387.4	1.8/ − 3.3
Eifelian	393.3	± 1.2	394.2	± 1.6	394.9	± 2.6
Emsian	407.6	± 2.6	407.9	± 1.0	407.6	4.3/ − 2.5
Pragian	410.8	± 2.8	414.4	± 1.1	411	± 3.5
Lochkovian	419.2	± 3.2	420	± 0.9	418.8	± 2.7

durations also being comparable. The main difference in results obtained by these two different methods is that the BChron 95% error bar width shows rapid fluctuations in its width. It contains about 10 local maxima in places of minimal density of occurrences of samples that were dated. Differences in error bar values are difficult to assess, but BChron assigns relatively large uncertainty where there is a lack of age dates around or on one side of the interpolated age of a stage boundary. In the latter case BChron appears to squeeze zones too much, in excess of their (thickness) duration uncertainty. The *R* cubic splining methods honor zonal stratigraphic uncertainty better, limiting how far a stage can expand in time. The mention of thickness in parenthesis just before the previous sentence is a reference to the fact that the Devonian position scale axis for the splines is derived from a subjective estimate of the duration of the Devonian zones and their link to the stage boundaries using relative thickness estimates. More information is provided by Becker et al. (Chapter 22: The Devonian Period, this book). The other Paleozoic periods, with the exception of the Cambrian that has no scaling of zones and stages, use different quantitative or semiquantitative methods for stratigraphic compositing to calculate a linear scale along the stratigraphic axis of events, zones, and stages. Hence, such a linear stratigraphic scale can be compared to the scale with radioisotopic ages in a two-way plot, using the splines, under discussion here.

14A.4 Statistical distribution of age determinations along the geologic time scale

How much weight should be given to the specific location of an age determination along the stratigraphic time scale? This is a philosophical question that suddenly has become important in GTS construction because of the conceptual modeling on which the BChron algorithm is based.

Conceptually, we believe that differences of expected frequency of age determinations per unit of geologic time probably exist. For example, the 29 $^{40}Ar/^{39}Ar$ bentonite dates of Obradovich (1993) for the Late Cretaceous do not seem to be uniformly distributed. Within the 65−100 Ma time interval, only 7 dates occur within the 65−82.5 Ma time interval versus 22 within the 82.5−100 Ma interval. If the bentonites that were dated would be randomly distributed over the entire 35 Myr time interval, the probability of it occurring in the younger time interval is 0.5. The probability that only 7 (of the 29) would occur within this interval becomes 0.0029 and the probability of 7 or fewer than 7 is 0.0041. Both these probabilities are less than 0.05 or 0.01. This suggests that there are probably fewer dates in the 65−82.5 Ma interval (and more in the 85.5−100 Ma interval) than expected for a random Poisson-type distribution. The probability of occurrence of a bentonite in the Late Cretaceous probably therefore depends on its age but how could we describe its time-dependent probability function?

In BChron the estimated probability of a predicted age being correct is relatively large at the place of occurrence of a dated rock sample and even somewhat larger if nearby there are other dated rock samples, but why? The Devonian time scale of Fig. 14A.2 is based on 18 irregularly distributed dates only. Any discrete statistical model to test for systematic changes in the number of dates per unit of time would not indicate significant clustering in time because sample size is too small. We could, however, look at differences between dates along the Devonian time scale. The following purely hypothetical example illustrates why this may provide a more promising approach. Suppose that in a large study area the same ash layer is sampled twice at locations that are relatively far removed from one another. The age determinations for these two ash samples will be different but they would have exactly the same position along the relative GTS. The probability that two age determinations would exactly coincide along the time scale is infinitesimally small. A definite result of this type could not be obtained from the original data when a Poisson-type model is used because the sample is too small. This is the reason that it will be good to look at first-order differences between locations of age determinations instead of at the locations themselves.

14A.4.1 Power-law models

Simple power-law models are often used for the construction of contour maps for noisy geochemical data irregularly distributed across a study area. The most popular model along these lines is quadratic with $\hat{y}_k = (1/n)\cdot \sum_{i=1}^{n} c_k \cdot y_{ik} \cdot d_{ik}^{-2}$ where the n values y_{ik} represent all observations located within a circular area with predefined radius around point k with estimated contour value $\hat{y}_k$ at its center, and d_{ik} is the distance between the points of occurrence of $\hat{y}_k$.and y_{ik}. In our application this isotropic squared deviation model can be used as follows. Every age determination y_k occurs at distance d_{ik} from other age determinations y_{ik} in its neighborhood. For example, the age determination y_k with value x_k along the geologic distance scale is distance d_{ik} removed from its closest neighbors with locations $x_{ik} = c_{ik}\cdot(x_k - x_{ik})^{-2}$. Use is made of the fact that x_{ik} already represents an estimate of y_{ik}. For convenience a simplified linear scale was used instead of original position along the stratigraphic scale. There is a linear relation between the stratigraphic scale of Fig. 14A.2 and the horizontal scale in Figs. 14A.3 and 14A.4 in which $x_k = 17$ represents sample D1 and $x_k = 136$ represents Cb1. The central point in Fig. 14A.3 with horizontal coordinate equal to 0 represents the point with $x_k = 17$. The six other points in

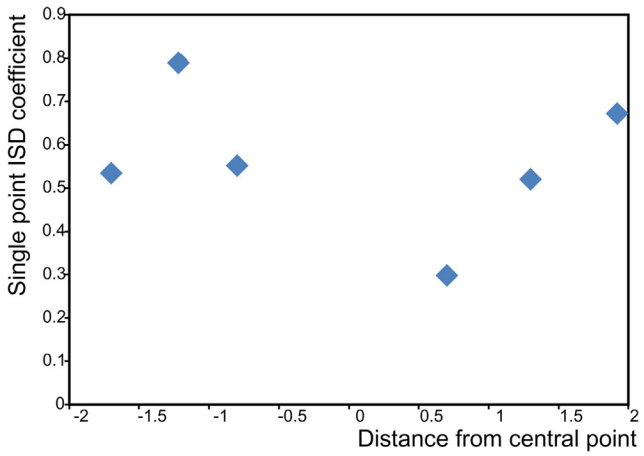

FIGURE 14A.3 Example of coefficients derived for quadratic power-law model connecting age determination with $x = 17$ to its three neighbors along the relative stratigraphic scale on each side (older and younger). Average coefficient of these six values is shown at point with Dev1 in Fig. 14A.2.

Fig. 14A.3 represent the three closest neighbors at either side of x_k. In order to reduce edge effects the series of 18 age determinations was enlarged at both the base and top of the Devonian using the end point reflection technique often used in time series analysis. If there would be no clustering of x_k values, all values c_{ik} would be realizations of the same random variable and independent of choice of x_k value with its neighbor's x_{ik}.

Averages of c_k values within selected neighborhoods would also be the same if the points would occur randomly. The average of the six c_{ik} values shown in Fig. 14A.3 is $c_k = 0.657$. Fig. 14A.4 shows similar average c_k values for all 18 x_k values. Standard deviations for all 18 6-point samples of relative ages were computed and multiplied by ± 1.96 to estimate 95% confidence limits for these average

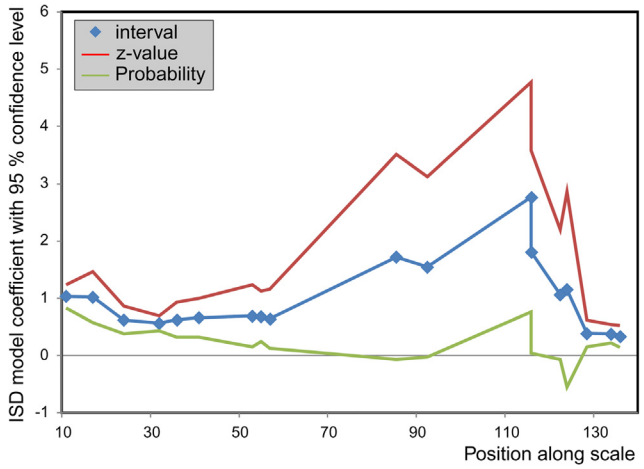

FIGURE 14A.4 Estimated coefficients for separate applications of quadratic power-law model at every sampling point along the relative geologic time scale with 95% confidence interval.

c_k values, which are also shown in Fig. 14A.4. Clearly there are significant differences between these values. It is noted that the version of the inverse square distance model used here is only applicable within relatively narrow neighborhoods. For x_k values within clusters of sampling points, wider neighborhoods could have been used; on the other hand, the choice of three neighbors on each side can be too wide for more isolated data points as illustrated by some points with unrealistic negative lower 95% confidence interval values shown in Fig. 14A.4. It can be concluded from the preceding exercise that the assumption of existing significant clustering in time of Devonian ages is reasonable. This tentative conclusion was confirmed to some extent in the following one-dimensional (1D) application of hot spot analysis.

14A.4.2 Hot spot analysis

Hot spot analysis (see, e.g., Getis and Ord, 1992) is widely applied by geographers to enhance two-dimensional (2D) patterns of random variables that exhibit spatial clustering. Typical examples are counts (x_{ij}) of occurrences (e.g., cases of a specific disease or accidents) for small areas (e.g., counties). Originally, the technique was based on Moran's I statistic for spatial correlation. It led to the Getis $G_i(d)$ statistic that satisfies:

$$G_i(d) = \frac{\sum_{j=1}^{n} w_{ij}(d)x_j}{\sum_{j=1}^{n} x_j}, \quad j \text{ not equal to } i,$$

where $\{w_{ij}\}$ is an asymmetric one/zero spatial weight matrix with ones for all links defined as being within distance d of a given i, all other links being zero (cf. Getis and Ord, 1992). Setting $W_i = \sum_{j=1}^{n} w_{ij}(d)$ it can be shown that the expected value of $G_i(d)$ and its variance satisfies:

$$E[G_i(d)] = \frac{W_i}{n-1}; \quad \sigma^2[G_i(d)] = \frac{W_i(n-1-W_i)Y_{i2}}{(n-1)^2(n-2)Y_{i1}^2}$$

where E denotes mathematical expectation, σ^2 is variance,

$$Y_{i1} = \frac{\sum_{j=1}^{n} x_j}{n-1}; \quad \text{and} \quad Y_{i2} = \frac{\sum_{j=1}^{n} x_j^2}{n-1} - Y_{i1}^2.$$

Although this technique was developed for 2D applications, it can be used in 1D as well. We simply have to think of a rectangular area in 2D that is being compressed onto a 1D line segment. It implies that all distances between points become positive. Assuming that $G_i(d)$ is approximately normally distributed, the standard normal random variable becomes:

$$Z_i = \left\{ G_i(d) - \frac{E[G_i(d)]}{\sigma[G_i(d)]} \right\}$$

In the application to the relative age locations along the x-axis of Fig. 14A.2, weights for all distances less than 6.0 were set equal to 1, and all other weights were

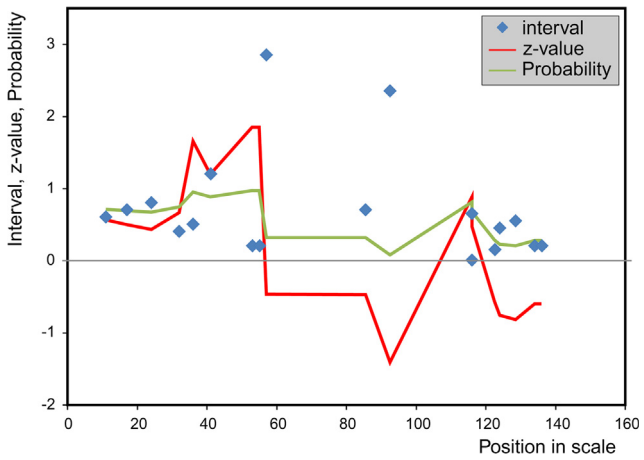

FIGURE 14A.5 Results of 1D hot spot analysis. Local neighborhoods of the age determination locations were used to estimate *z*-values, which are shown together with their standard normal probabilities. *1D*, One-dimensional.

set equal to zero. Application of the preceding equations then results in the *z*-values graphically shown in Fig. 14A.5. Locally these *z*-values almost reach the 95% confidence limit. It is noted that in Fig. 14A.5 the same vertical scale is used for different quantities. As in the previous exercise that resulted in Fig. 14A.4, the possibility of clustering of ages along the horizontal scale is indicated. It is noted that anticlustering locally is statistically significant at the 0.05 level of significance in the vicinity of the Givetian where density of age determinations is at its lowest. Later (see Section 14A.5.1) this fact will be used to modify the width of the 95% confidence belt on the best fitting smoothing spline. It is also noted that the *z*-values and probabilities in Fig. 14A.5 show downward trends at the beginning and the end. These are end point effects that could have been reduced to some extent by application of the 1D end point reflection technique used to construct Fig. 14A.4.

14A.4.3 Clustering of ash beds

It seems worthwhile to recognize age clustering as a third source of uncertainty (in addition to the radioisotopic 2-sigma error and stratigraphic uncertainty) and to incorporate it in the time scale construction procedure. Of course, this is already done automatically when BChron is used. This procedure would involve relatively increasing the weights for age determinations occurring within clusters as will be done in Section 14A.5.5.

It seems that the local maximal precision estimates coinciding with single dates or clusters of observed dates in the BChron solution would suggest that the positions of the samples that were taken are somehow special. It is better to consider the positions of the samples within the periods not as special but as purely random although these positions are probably subject to some clustering in time.

14A.5 Modifications in GTS2020

Essentially, statistical treatment of GTS2020 age data for Paleozoic periods or two successive periods is similar to the methodology described in Sections 14A.2.2 for treatment of Paleozoic age determinations in GTS2004 and in Section 14A.3.5 for treatment of the GTS2012 Devonian age data. A major difference between the Ordovician–Silurian and Carboniferous–Permian age databases contrary to the Devonian database is that there are many more age determinations that are more or less equally spaced and without significant (listed) stratigraphic uncertainty. This improvement of the radioisotopic database is noticeable at the boundaries between periods at which different methods were employed to construct the stratigraphic scales. Incorporation of some dates from neighboring older or younger periods can help to overcome problems of this type provided that stratigraphic scales at both sides of a period boundary are constructed by means of the same method. In GTS2004 such discrepancies at stage boundaries were eliminated by the rather imprecise method of "ramping." Estimation of the ages of the Paleozoic stage boundaries will be based on smoothing splines obtained by means of the *R smooth-spline* technique with CV. Successive spline curves fitted to different data sets may result in two slightly different ages for the same period boundary. Two age estimates then can be combined with one another by computing their weighted average as discussed in the next section.

14A.5.1 Combining dates at the same stratigraphic level

Suppose that y_i and y_{i+1} are two successive values with the same *x*-value. Their approximate 95% confidence interval can be written as $2 \cdot \sigma(y_i)$ and $2 \cdot \sigma(y_{i+1})$. From these two values the weights of the two observations can be computed as $w_i = 1/\sigma^2(y_i)$ and $w_{i+1} = 1/\sigma^2(y_{i+1})$. The sum of these two weights can be written as $w(x) = w_i + w_{i+1}$ where *x* represents location of both y_i and y_{i+1} along the *x*-axis. The same procedure can be followed when more than two dates have the same value of *x*. If there are two dates only, their weighted average is:

$$y_x = \frac{w_i y_1 + w_{i+1} y_{1+1}}{w(x)}.$$

Again, the same procedure can be followed if there are more than two dates with the same value of *x*. Application of this procedure to the GTS2020 age

determinations for the Devonian reduces the total number of dates from 31 to 19.

The preceding statistical procedure also can be used for combining two different estimates at a series boundary. For example, the spline curves for the Devonian and the Carboniferous–Permian produced slightly different estimates for base Tournaisian (358.8 ± 0.7 and 359.9 ± 0.4 Ma, respectively). The weighted average of these two estimates (359.3 ± 0.3 Ma) is probably the best estimate of the age of the base of the Carboniferous. It is somewhat closer to 359.9 Ma with less uncertainty than 358.8 Ma.

14A.5.2 Smoothing splines

In our GTS2020 applications use was made of the *R*-program *smooth-spline* as implemented by B.D. Ripley and M. Maechler in *R*.Stats Package version 3.6.0, with uncertainties based on total variances $s_t^2(y)$ instead of on s^2 (y) gave the result shown in Fig. 14A.2. This program is freely available on the Internet and widely used. Originally, the technique used now was based on code in the GAMBIT FORTRAN program by Hastie and Tibshirani (1990) using a smooth-spline function similar to the one described in Chambers and Hastie (1992).

The default application in *R smooth-spline* is application of a technique called generalized CV (GCV). This technique was originally introduced by Wahba (1985) as a possible refinement of leaving-one-out CV. Differences between CV and GCV are discussed by Wang (2011). Usually the two methods give approximately the same results. However, in several of our applications to Paleozoic data sets, CV provided better results than GCV. This is because it is more robust in situations that relatively many points along the *x*-axis are close together or coinciding, even after application of the weighted average method described in the previous section. In such situations, CV produces a smooth curve, whereas the GCV result may reduce to a set of straight-line segments connecting neighboring points. Best fitting smooth curves were obtained by CV in all Paleozoic applications. Because of scarcity of dates for the Devonian, the spline curve for this period has more uncertainty associated with it than the spline curves for the other periods.

It is noted that in some of our *smooth-spline* applications the initial output contained a warning that results (automatic *smooth-spline* estimation of CV) were not necessarily accurate because locally one or more successive *x*-values were equal or nearly equal to one another. In such situations, we have combined successive values (with the same position along the stratigraphic axis) with one another so that the *smooth-spline* warning sign would disappear. The method used to combine successive values was explained in the previous subsection.

The GTS2020 Devonian smoothing spline derived by CV (see Becker et al., Chapter 22: The Devonian Period, this book) closely resembles Fig. 14A.2. It also resembles the GTS2012 bootstrap spline modified by connecting the dates for samples D7 and D9 with the straight-line segment. Moreover, the spline of Fig. 14A.2 is intersected by the 2-sigma error bars of all input dates except those for dates D5 and D13/D14A. In general, uncertainties in age determinations can be shown as crosses that are ± 2-sigma in height for the age determinations and have widths equal to those of the stratigraphic uncertainty boxes. The resulting uncertainty crosses provide a simple check on how well the original data are in accordance with the best fitting spline curve. On average one would expect that only about 5% of these crosses do not intersect the curve. This simple approximate goodness-of-fit test will be passed by all GTS2020 Paleozoic period spline curves fitted by us but not for the Early Cretaceous spline as will be discussed later in this chapter.

Curve fitting for the other Paleozoic periods is rather straightforward in that various techniques (smoothing spline, polynomial regression, or LOESS) yield more or less the same solution. Moreover, 2-sigma values for successive age determinations are similar and it is possible to interpolate between these values to obtain reasonably good estimates of the 95% confidence intervals for the estimated stage boundary ages.

14A.5.3 Application to the Ordovician–Silurian

As previously for GTS2012 constrained optimization (CONOP) values for graptolites in the Ordovician and Silurian periods were obtained by Peter Sadler for GTS2020 (cf. Section 14A.2) as a basis for time scale estimation on a scale from 1 to 100 composite units. CONOP scale duration of the two periods is about 85 composite units. Similar data are available for Ordovician conodonts. The combined duration of these two periods is about 68 Myr. Thus one composite unit is equivalent to about 0.8 Myr. As for GTS2012, smoothing splines were obtained by relating the dates for both periods combined with one another to the CONOP values. Numbers of dates used were 51 for the Ordovician and Silurian graptolites and 24 for the Ordovician conodonts. For both Ordovician–Silurian graptolites and Ordovician conodonts, the number of dates for which CONOP values are available exceeds the number of dates in Table 14A.2.

The best fitting spline curves for graptolites and conodonts are shown in Figs. 14A.6 and 14A.9, respectively. Spline-curve estimates of the Ordovician and Silurian stage boundaries are shown in Table 14A.2. In the period chapters the same spline curves are shown along with the error bars for the age determinations (Fig. 20.15C in Goldman et al., Chapter 20: The Ordovician Period, this book). Results for the Ordovician and Silurian graptolites were

TABLE 14A.2 Estimates of Ordovician–Silurian stage boundary ages.

	Graptolites		Conodonts	
Base of Stage	Spline	2-sigma	Spline	2-sigma
Lochkovian	419.00	1.77		
Pridolian	422.73	1.62		
Ludfordian	425.01	1.53		
Gorstian	426.74	1.47		
Homerian	430.62	1.32		
Sheinwoodian	432.93	1.24		
Telychian	438.59	1.05		
Aeronian	440.49	0.99		
Rhuddanian	443.07	0.91		
Hirnantian	445.21	0.86	446.16	1.63
Katian	452.75	0.73	452.98	1.45
Sandbian	458.18	0.73	458.76	0.79
Darriwilian	469.42	0.93	470.40	0.71
Dapingian	471.26	0.98	473.93	0.90
Floian	477.08	1.17	478.72	1.21
Tremadocian	486.45	1.53	487.20	1.83

accepted for GTS2020. The results for conodonts shown in Fig. 14A.9 were not used for GTS2020. Two-sigma values for the stage boundaries (also shown in Table 14A.2) were estimated in two steps. First, approximate 95% half-confidence limits were estimated for the spline curve for graptolites according to the method to be explained in Section 14A.5.5 for the Devonian where the approach will be taken a step further to account for probable lack of ash layers in the Givetian. It is noted that in the spline-curve fitting every age determination was weighted according to the inverse of its variance, which is the square of its sigma value. These weights are shown in Fig. 14A.7. The 95% half-confidence interval for the Ordovician and Silurian graptolites is shown in Fig. 14A.8.

CONOP values for graptolites and conodonts in the Ordovician–Silurian are not directly comparable with one another, because time scales based on them are significantly different as can be seen from Figs. 14A.6 and 14A.9 in which the spline curves have different shapes. However, both spline-curve values for CONOP values of graptolites and conodonts provide stage boundary age estimates for the same single event and, therefore, could be averaged by combining the two separate uncertainty estimates with one another in a second step. A method for this type of averaging can be based on elementary statistical theory. It differs from the weighted average calculation procedure presented in Section 14A.5.1. The overall mean value for stage boundary estimates satisfies:

$$\overline{y} = \frac{n_g \cdot \overline{y_g} + n_o \cdot \overline{y_o}}{n_g + n_o}$$

where n_g and n_o are numbers of dates for graptolites and conodonts representing weights for the two age estimates ($\overline{y_g}$ and $\overline{y_o}$) for any stage boundary. The corresponding 2-sigma values then can be derived from the sample variances for graptolites and conodonts that can be written as s_g^2 and s_o^2, respectively. The 2-sigma value of the overall mean value follows from the pooled variance that satisfies:

$$s^2 = \frac{(n_g - 1)\cdot s_g^2 + (n_o - 1)\cdot s_o^2}{n_g + n_o - 2}.$$

Table 14A.2 shows separate estimates of Ordovician stage boundaries only. It could be assumed that averaging the stage boundary estimates obtained by two different methods for the Ordovician provides better estimates than those obtained by using time scales based on graptolites and conodonts separately. However, conodont uncertainties are significantly larger than graptolite uncertainties and it was decided to base the GTS2020 Ordovician–Silurian time scale on graptolites only as was done for GTS2012.

14A.5.4 Application to the Devonian

At several locations GTS2020 age data for the Devonian have two or more age determinations with the same values (and their uncertainties) along the stratigraphic scale (x-axis). The reason for this is that at these locations more than one a single ash layer was sampled. More than one y-value with the same x-value can present a problem for some techniques of curve fitting. For example, in BChron output, strong and rapid fluctuations that are not realistic may arise near such locations. In spline-curve fitting with CV, which is our preferred method for time scale construction, successive points along the x-axis are connected by cubic polynomials that each have four coefficients. Obviously, a cubic polynomial cannot be estimated when two successive ages have the same x-value. The *R* smooth-spline program attempts to take care of situations of this type but issues a warning that the final smoothing spline is not necessarily correct. In order to avoid possible problems of this type, we have computed weighted averages for Devonian age determinations with the same x-value (Fig. 14A.10) according to the method given in Section 14A.5.1. The resulting spline curve for Devonian is in Fig. 22.14 of Chapter 22, The Devonian Period (this book).

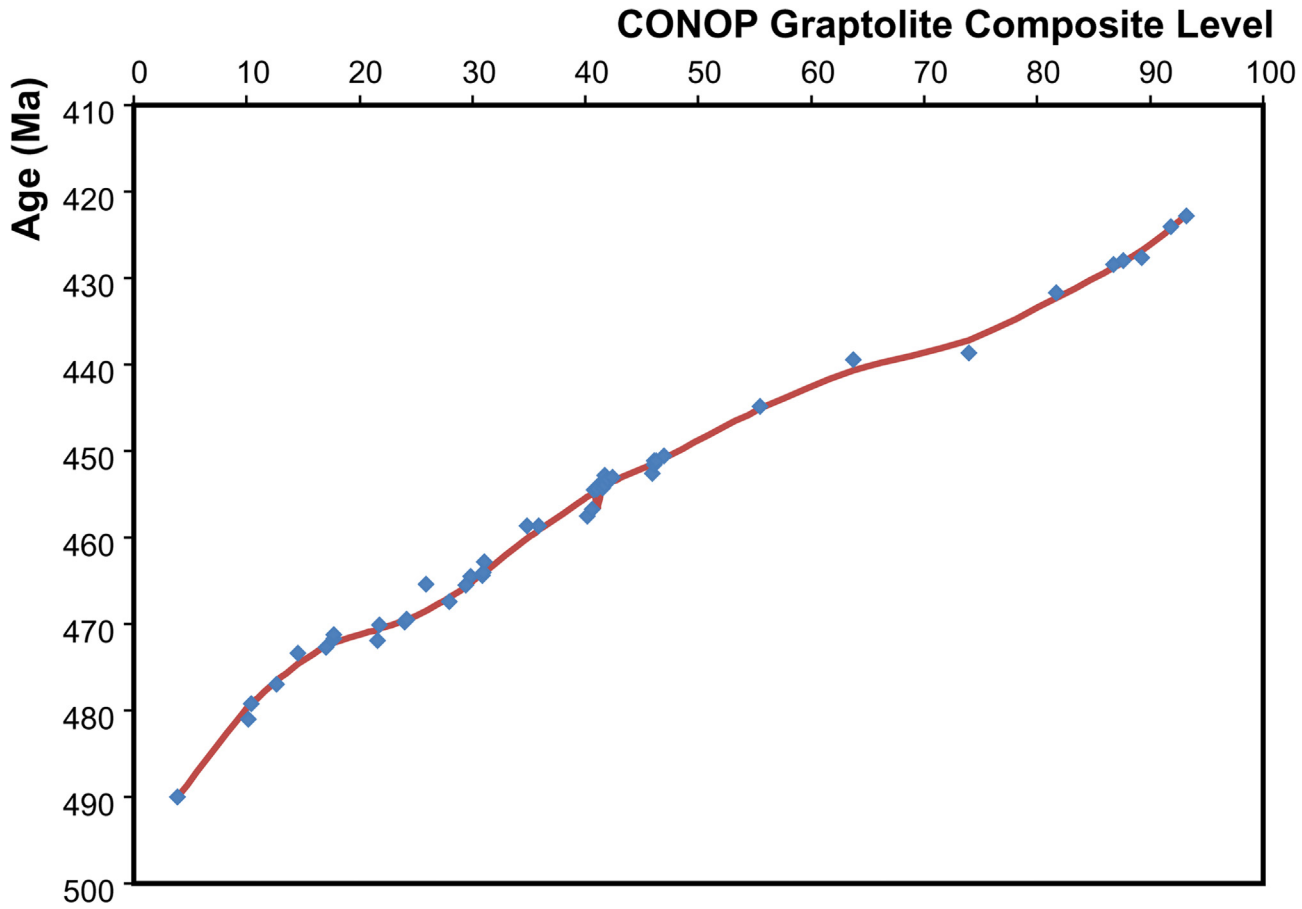

FIGURE 14A.6 Best fitting spline curve for the composite of the Ordovician–Silurian graptolite ranges and events.

It is noted that the Devonian spline curve that was fitted to the input data gave estimated ages of 358.7 and 420.6 Ma for top and base of the Devonian, respectively. However, these two estimates deviate slightly from estimates obtained by means of spline fitting for the Carboniferous–Permian (cf. Fig. 14A.12) and Ordovician–Silurian (cf. Table 14A.2).

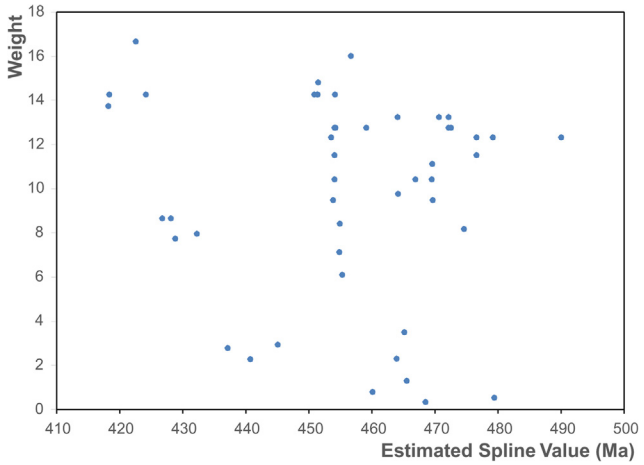

FIGURE 14A.7 Weights of Ordovician-Silurian graptolite age dates as a function of estimated spline values.

By using the method of averaging two different estimates for the same stratigraphic event, the estimated age for top of the Devonian was revised to 359.3 Ma. The final GTS2020 age and error for Silurian–Devonian boundary value (419.0 ± 1.8 Ma) is taken from the Ordovician–Silurian data and spline fit, using a more updated data set for Ludfordian–Pridoli stage intervals than used in the slightly earlier "crunched" Devonian ages (Brad Cramer, pers. comm. to F. Gradstein, August 2019).

As shown in Section 14A.4, some clustering of GTS2012 Devonian dates along the *x*-axis (or *y*-axis) probably exists. For example, the lack of bentonite layers between upper Eifelian and lower Frasnian is probably real. For this reason an approximate method can be used to obtain 95% confidence intervals for the estimated stage boundary ages shown in Fig. 14A.11. Although the Devonian spline curve is not a straight line, the deviations from this curve at the sampling point locations may be assumed to maintain equal variance along the line. Fig. 14A.10 shows the 19 Devonian weights plotted against the estimated smoothing spline value. The best fitting straight line in this diagram is almost horizontal indicating that the weights are approximately constant during the entire Devonian period.

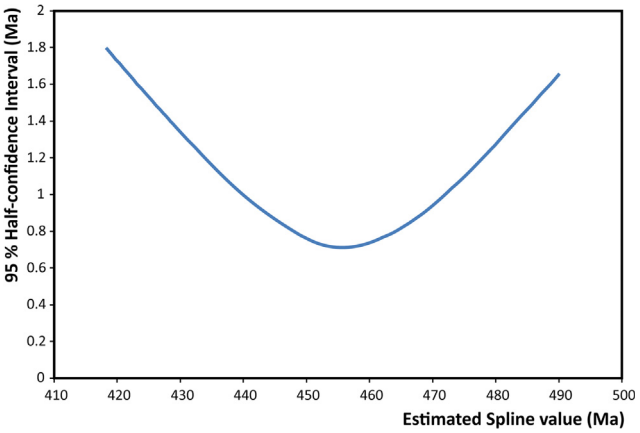

FIGURE 14A.8 Two-sigma values for estimated spline-curve for Ordovician-Silurian graptolites shown in Figure 14A.6.

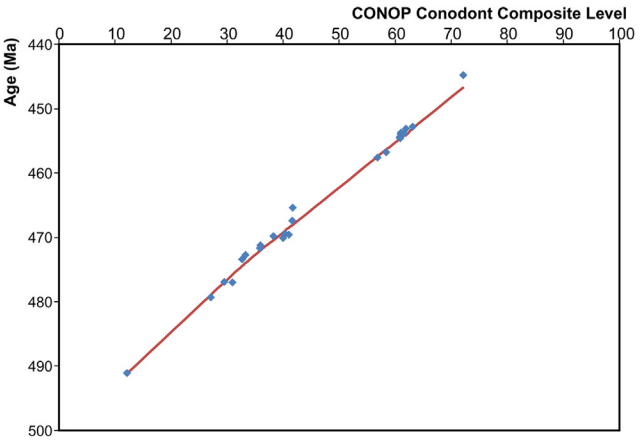

FIGURE 14A.9 Best-fitting spline-curve for the composite of Ordovician-Silurian conodont events and ranges.

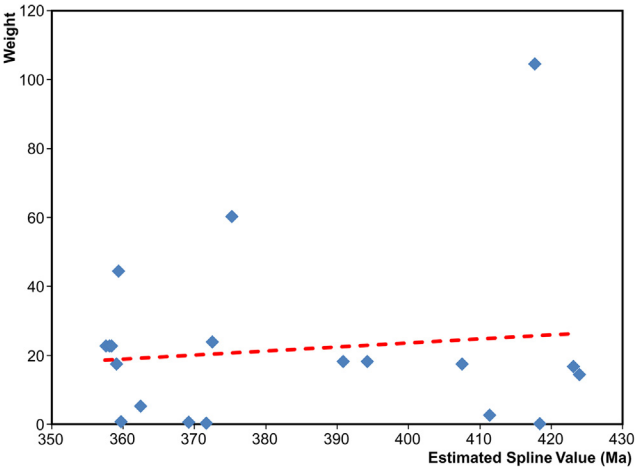

FIGURE 14A.10 Weights of Devonian dates as a function of estimated spline values.

14A.5.5 New approximate Devonian 95% confidence interval

As mentioned before, the procedure of Paleozoic time scale construction followed in GTS2004 was based on the idea that a plot of the observed age determinations against the estimated spline ages is approximately according to a straight line with the simple equation $y = x$. This procedure is equivalent to the method originally used by McKerrow et al. (1985) and Cooper (1999). The 95% confidence belt for this line at any point (x_k, y_k) satisfies:

$$y_k \pm t(n-2)\cdot s_e\sqrt{1-R_k}$$

where

$$R_k = (1/n) + \left(\{x_k - (\sum x_k/n)\}^2 / \sum\left((x_k - (\sum x_k/n)\right)^2\right)$$

(cf. Agterberg, 1974, Equation 8.31).

The total number of observations $n = 19$ and Student's t $(17) = 2.11$. There are two ways in which the standard deviation s_e can be calculated: weighted or unweighted. In the weighted method, which is to be preferred, every age determination is weighted according to the inverse of its variance. In the unweighted method, all age determinations are given equal weights. In the current application the weighted method was used. Fig. 14A.11 shows the 95% half-confidence belt for the Devonian as a solid line. The same procedure was used for the Ordovician–Silurian graptolite graph shown in Fig. 14A.6. For the Devonian the approach is taken one step further to account for the probable variations in density of sampling points in this period.

Suppose that m_k for point k is the number of other observations within a time interval of 10 Myr. The maximum number of other observations within a time interval of 10 Myr is $\max(m_k) = 7$. Density of observations for point k can be set equal to $d_k = m_k/\max(m_k)$. The reciprocal of is measure of

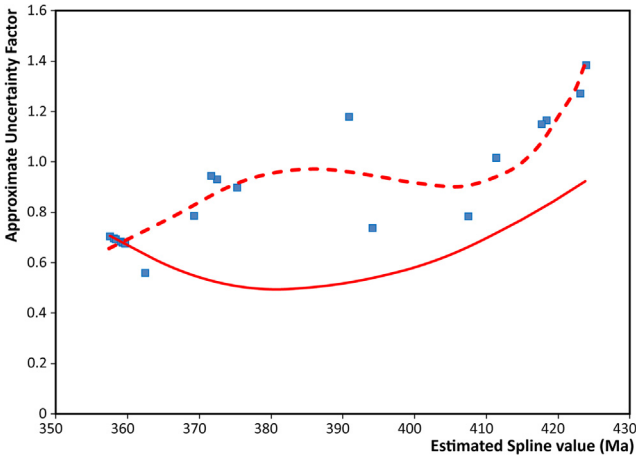

FIGURE 14A.11 Approximate uncertainty factor used to widen 95% confidence belt incorporating changes of density of dates along the Devonian time scale.

density provides a measure of sparseness of observations at any data point. Dividing the values of the 95% half-confidence interval results in the values shown in Fig. 14A.11 as solid squares. These values fall approximately on the broken line also shown in this figure. This broken line provides approximate 95% confidence intervals for the estimated ages of the GTS2020 Devonian stage boundaries shown in Table 14A.1. In addition to the increases in uncertainty toward top and base of the Devonian, Fig. 14A.11 also shows more uncertainty at top and bottom of the Givetian where there is a relative lack of age determinations. The preceding procedure for the Devonian remains approximate and speculative because of lack of information.

Table 14A.3 shows a comparison of the GTS2020 Devonian age determinations with their estimated spline values. The weights (W) in this table were determined by both the original 2-sigma values of the age determinations and the stratigraphic uncertainties as explained previously. Age determinations with the same position along the stratigraphic scale were averaged, which involved relative weight increases. The uncertainties ($2\sigma'$) of the spline values were estimated according to the same method used for estimating the uncertainties of the Devonian stage boundary ages.

Stratigraphic uncertainty for the age determinations is commonly represented as a rectangular box of which the base here is written as q. For the Devonian this uncertainty is graphically represented as a horizontal line segment with length q. From statistical properties of the rectangular frequency distribution summarized in Section 14A.2.1, it follows that $q = 3.48 \cdot s_q(x)$ where $s_q(x)$ is the standard deviation of this rectangular frequency distribution. The weight (W) in Table 14A.3 satisfies $W = 1/s_t^2$ where s_t^2 is the variance of total uncertainty, which satisfies $s_t^2 = s^2 + s_q^2$ in which s^2 represents variance of the age determination. Consequently, q can be derived from $s_q^2 = W^{-1} - s^2$. Stratigraphic uncertainty will also be considered in this way for the Early Cretaceous (Table 14A.4). It is noted that in Table 14A.3 and similar tables, in which original age determinations or averages of age determinations with the successive data points along the stratigraphic axis are compared with estimated spline values, the weights W are significantly different

TABLE 14A.3 Columns 1–3 list the latest Silurian through earliest Carboniferous radioisotopic age dates with their 2-sigma uncertainties for calculation of the Devonian geologic time scale, and columns 4–7 list the corresponding estimated spline values and ages; $2\sigma'$ represents estimated spline value uncertainty.

Sample number and Radioisotopic Age			Spline used for GTS2020			
No.	Age (Ma)	2σ	x-Axis	weight	Age (Ma)	$2\sigma'$
CB3	357.26	0.42	356.9	15.4	357.57	0.87
CB2	358.43	0.42	357.9	17.4	358.07	0.85
CB1	358.71	0.42	358.5	21.1	358.35	0.85
D27	358.89	0.48	360.1	15.4	359.05	0.84
D25/D26	359.11	0.3	360.7	38	359.34	0.84
D24	361.3	2.4	361.3	0.5	359.68	0.83
D22/D23	363.06	0.88	365.2	3.2	362.42	0.68
D21	367.7	2.8	374	0.4	369.23	0.98
D19	372.36	0.41	377.6	13.9	372.49	1.15
D20	374.2	4.2	376.7	0.2	371.64	1.16
D17/D18	375.32	0.26	380.5	52.3	375.25	1.1
D14/D15	390.47	0.34	395.2	18.2	390.84	1.45
D13	394.29	0.47	397	17.1	394.19	0.91
D12	407.75	1.16	403.8	2.9	407.52	0.97
D10/D11	411.64	0.88	408	3.3	411.38	1.27
D9	415.6	0.8	412	2	418.36	1.37
D1/D8	417.53	0.19	415	29.5	417.7	1.42
S8	422.91	0.49	421.8	9.4	423.1	1.57
S7	424.08	0.53	423.3	11	423.93	1.72

from one another. However, unless the spacing between successive points along the stratigraphic axis is markedly uneven as for the Devonian, estimated spline values are relatively insensitive to differences in W. The estimated spline values then are not significantly different from those obtained after setting are weights W equal to one.

14A.5.6 Application to the Carboniferous–Permian

The input data for the Carboniferous and Permian differ from those of the earlier Paleozoic periods in that uncertainties are much smaller. Fig. 14A.12 (also shown in Fig. 23.8 of Chapter 23: The Carboniferous Period, this book) shows that the best fitting spline curve almost exactly follows the input data. For this reason the original 2-sigma values where accepted to express the 95% confidence limits of the estimated ages on the spline curve as well.

Table 14A.4 shows a comparison of the GTS2020 Carboniferous–Permian age determinations with their estimated spline values. The weights (W) in this table were determined by both the original 2-sigma values of the age determinations. In comparison with other periods there is relatively little difference between the age determinations and the spline values. Uncertainties of Carboniferous–Permian stage boundary age estimates in GTS2020 were determined by the original 2-sigma values of the age determinations.

14A.5.7 Application to the Early Cretaceous

Spline fitting as applied to Paleozoic periods in GTS2020 was also used to help obtain the GTS2020 Cretaceous time scale. The critical factor for the Early Cretaceous scale in GTS2020 is that a rather high-resolution U–Pb radioisotopic and cyclostratigraphic data set is now available for the Tithonian through Barremian, which is quite different than the values used during the construction of GTS2012 (see discussions in Chapter 5: Geomagnetic Polarity Time Scale, and in Chapter 27: The Cretaceous Period, this book).

Fig. 14A.13 is a plot of radioisotopic dates against mid-km M-sequence magnetic anomaly distances that span ca. 1200 km in total (see Table 5.4 in Chapter 5: Geomagnetic Polarity Time Scale, this volume). In order to incorporate stratigraphic uncertainty, $s(x)$ was estimated for each distance value (x) by multiplying its sigma value

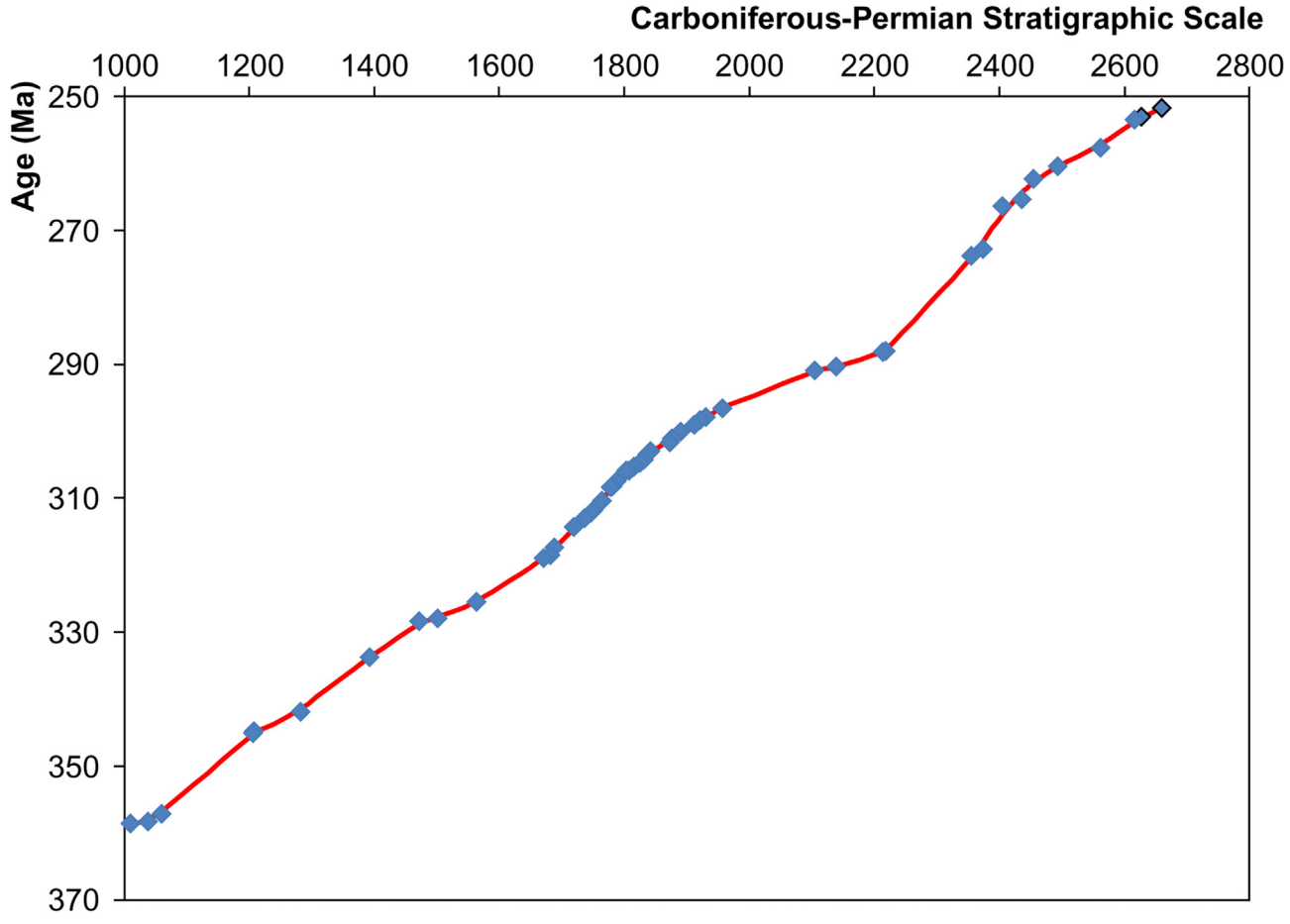

FIGURE 14A.12 Best-fitting spline-curve for the Carboniferous-Permian.

TABLE 14A.4 Comparison of composite standard age determinations for the Carboniferous–Permian with estimated spline values.

Radioisotopic age			Spline			Radioisotopic age			Spline		
No.	Age (Ma)	2σ	*x*-axis	Weight	Age (Ma)	No.	Age (Ma)	2σ	*x*-axis	Weight	Age (Ma)
P37	251.94	0.28	2658.97	51.02	251.81	CB40	304.83	0.36	1823.94	30.86	304.72
P24	253.24	0.45	2627.25	19.75	253.31	CB38	305.51	0.39	1815.63	26.22	305.36
P23	253.60	0.29	2616.07	47.56	253.92	CB37	305.95	0.37	1808.17	29.22	305.96
P22	257.79	0.31	2561.00	41.62	257.38	CB36	305.96	0.36	1803.58	30.86	306.35
P17	260.57	0.31	2493.70	41.62	260.59	CB35	307.66	0.37	1787.42	29.22	307.84
P16	262.45	0.37	2455.10	29.22	262.98	CB33	308.36	0.38	1781.19	27.70	308.47
P14	265.46	0.39	2435.07	26.30	264.68	CB32	308.50	0.36	1778.65	30.86	308.73
P13	266.50	0.37	2405.00	29.22	267.80	CB30	310.55	0.38	1764.26	27.70	310.24
P11	272.90	0.34	2374.00	34.60	271.84	CB29	312.01	0.37	1749.94	29.22	311.74
P9	274.00	0.34	2354.18	34.60	274.37	CB28	312.23	0.37	1746.73	29.22	312.07
P8	288.21	0.34	2218.44	34.60	288.04	CB27	313.16	0.37	1736.65	29.22	313.08
P7	288.36	0.35	2213.92	32.65	288.29	CB24	314.40	0.37	1719.12	29.22	314.77
P6	290.81	0.35	2133.26	32.65	290.66	CB23	317.54	0.38	1688.24	27.70	317.65
P5	290.50	0.35	2138.88	32.65	290.56	CB21	318.63	0.40	1681.38	25.00	318.23
P4	291.10	0.36	2104.31	30.86	291.22	CB20	319.09	0.38	1670.76	27.70	319.13
P3	296.69	0.37	1956.62	29.22	296.69	CB18	325.64	0.40	1563.00	25.00	325.58
P2	298.05	0.56	1931.16	12.76	298.04	CB14	328.14	0.40	1501.14	25.00	327.87
P1	298.49	0.37	1921.55	29.22	298.57	CB12	328.48	0.41	1472.00	23.80	328.97
CB47	299.22	0.37	1912.24	29.22	299.10	CB10	333.87	0.39	1392.63	26.30	333.87
CB46	300.22	0.35	1889.68	32.65	300.43	CB6	342.01	0.41	1281.96	23.80	341.58
CB45	301.29	0.36	1876.25	30.86	301.25	CB5	345.00	0.40	1208.19	25.00	345.27
CB44	301.82	0.36	1873.47	30.86	301.42	CB4	345.17	0.41	1206.37	23.80	345.39
CB43	303.10	0.36	1842.09	30.86	303.41	CB3	357.26	0.42	1059.84	22.68	356.94
CB42	303.54	0.39	1837.87	26.30	303.70	CB2	358.43	0.42	1037.63	22.68	358.10
CB41	304.49	0.36	1830.75	30.86	304.21	CB1	358.71	0.42	1010.44	22.68	359.16

by the ratio of total time interval (=47.8 Myr) and the span of 1200 km in order to make use of the total variance equation: $s_t^2(y) = s^2(x) + s^2(y)$ (cf. Section 14A.2.1). The resulting smoothing spline, which is also shown in Fig. 14A.13, is almost exactly a straight line representing constant seafloor spreading. The corresponding weights $w_t = 1/s_t^2(y)$ are given in Fig. 14A.14 and the deviations themselves are shown in Fig. 14A.15. These deviations are very small. The spline curve in Fig. 14A.13 (also in Figs. 5.4 and 27.10 of Chapter 5: Geomagnetic Polarity Time Scale, and Chapter 27: The Cretaceous Period, this book) is approximately a straight line with the equation $y = 0.0372x + 122.77$, a result that can also be obtained by using the method of ordinary least squares. This would imply a constant spreading rate for the Late Jurassic through Barremian portion of the M-sequence. Degree of fit for this line could not be improved significantly by including higher order terms in the polynomial equation fitted by the method of least squares.

Mid-km M-sequence magnetic anomaly distances assigned to stage boundaries are given in column 2 of Table 14A.5 with the corresponding ages in column 3. It is noted that in Fig. 14A.13 contrary to the Devonian period applications shown in Figs. 14A.2 and 14A.10, and similar figures for the other Paleozoic period applications, relatively many uncertainty crosses do not intercept the

TABLE 14A.5 Callovian–Cenomanian spline-curve age estimates adjusted for Milanković-based stage duration estimates. Final age estimates, 2-sigma values and revised stage durations are provided in last three columns.

		M-Sequence Spline			Cycles Spline			Final Age		
Base of Stage	M-Sequence Distance (km)	Spline Age	2-Sigma	Duration	Milankowić cycle duration (Myr)	duration-2	Age-2	Revised Age	2-Sigma	Revised duration
Cenomanian		~100.5	0.14				100.5	100.5	0.1	
Albian		~113.1	0.3	12.6	12.45	12.84	113.34	113.2	0.3	12.7
Aptian	0	122.77	0.9	9.67	8.1	8.35	121.69	121.4	0.9	8.2
Barremian	120	127.23	0.78	4.46	5	5.16	126.85	126.5	0.8	5.1
Hauterivian	198	130.13	0.72	2.9	5.93	6.12	132.96	132.6	0.7	6.1
Valanginian	347	135.67	0.63	5.54	5.06	5.22	138.18	137.7	0.6	5.1
Berriasian	523	142.21	0.62	6.54	5.27	5.43	143.62	143.1	0.6	5.4
Tithonian	701	148.82	0.71	6.61	5.67	5.85	149.46	148.9	0.7	5.8
Kimmeridgian	845.2	154.18	0.84	5.36	5.2	5.36	154.83	154.8	0.8	5.9
Oxfordian	1013.69	160.44	1.03	6.26	5.8	5.98	160.81	160.8	1	6
Callovian	1082.58	163	1.11	2.56	3	3.09	163.9	163.9	1.1	3.1

After final stratigraphic evaluation selected uncertainties were slightly decreased. See text in Chapter 27, for further explanation.

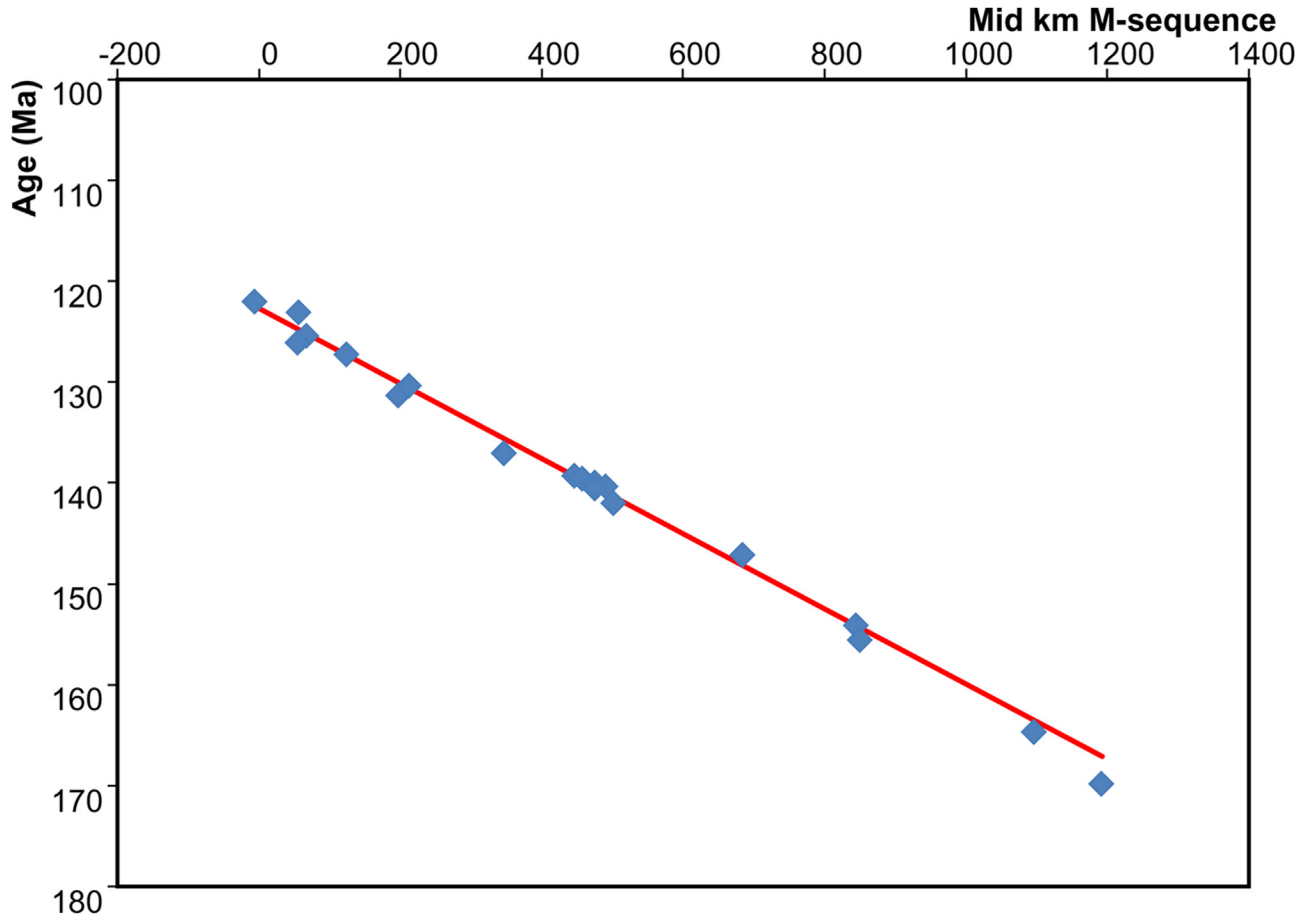

FIGURE 14A.13 Best fitting spline curve for the Early Cretaceous.

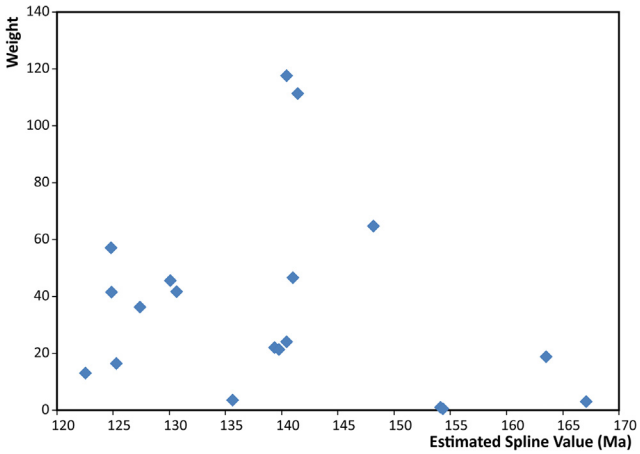

FIGURE 14A.14 Weights of Early Cretaceous dates as a function of estimated spline values.

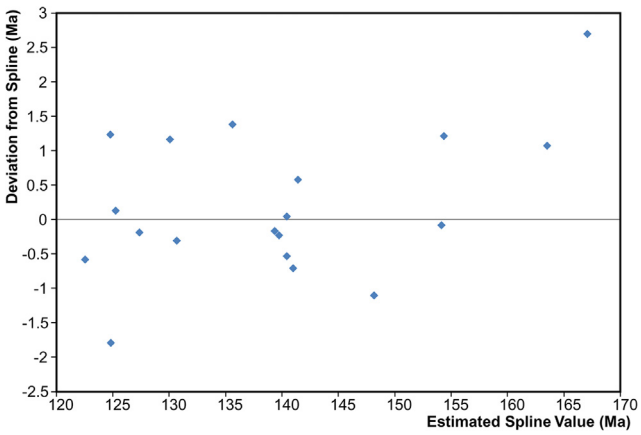

FIGURE 14A.15 Deviations of input ages from spline curve of Fig. 14A.13.

best fitting cubic spline curve. A probable explanation of this fact is that the reported 2-sigma values of the age determinations are systematically too low. Nearly all uncertainties in the mid-km M-sequence magnetic anomaly values are negligibly small. In GTS2004 Appendix 3 (Agterberg, 2004) it was pointed out that, if all standard deviations of the dependent variable all too small by a factor c, the estimates of the two coefficients of the best fitting straight line remain unbiased. It is only that their standard deviations, and their covariance, are underestimated by the factor c. The doubly hyperbolic 95%

TABLE 14A.6 Comparison of marine magnetic anomaly M-sequence age determinations with estimated spline values; $2\sigma'$ represents estimated spline value uncertainty.

M-sequence			Spline		
M-sequence (km)	Age (Ma)	2σ	Weight	Age (Ma)	$2\sigma'$
−4.9	122.01	0.52	12.96	122.60	0.52
57	123.10	0.30	41.51	124.90	0.51
68.5	125.45	0.43	16.39	125.33	0.51
55.8	126.07	0.25	56.98	124.86	0.51
125.5	127.24	0.25	36.16	127.45	0.51
198	131.29	0.25	45.48	130.15	0.51
213.5	130.39	0.25	41.59	130.72	0.51
347	137.05	1.00	3.54	135.69	0.53
447.8	139.24	0.16	22.03	139.44	0.56
457.7	139.55	0.18	21.24	139.81	0.56
476.9	139.96	0.17	24.02	140.53	0.57
491.8	140.34	0.18	46.55	141.08	0.58
476.3	140.51	0.16	117.59	140.50	0.57
500	146.48	1.63	1.48	141.50	0.58
503	142.04	0.17	111.37	141.39	0.58
684.7	147.11	0.18	64.71	148.26	0.68
845.2	154.10	2.10	0.90	154.23	0.80
851	155.60	0.89	0.49	154.45	0.80
1097.9	164.64	0.27	18.74	163.63	1.05
1193.3	169.80	1.15	3.01	167.18	1.17

confidence interval on the best fitting straight line also would be biased (by the factor c). In order to avoid this problem and to obtain 2-sigma values of the stage base estimates, we have followed the simple alternative method described previously (see section on estimation of approximate 95% Devonian confidence interval) by assigning equal weights to all data points plotted in Fig. 14A.13.

Already Kent and Gradstein (1985) in their Cretaceous and Jurassic geochronology study for the Decade of North America Geology publications arrived at constant and linear spreading of the M-sequence as a reasonable template to interpolate the Oxfordian through Barremian time scale. Despite use of few tie points for the age versus M-sequence km plot, the Jurassic−Cretaceous boundary was interpolated by Kent and Gradstein (1985, 1986) at 144 Ma, although they used a different working definition for that period boundary. This is only slightly older than current proposed placement of that boundary relative to the M-sequence, which would project to an age of 142.3 Ma from the direct spline fit of radiometric dates to magnetic anomalies and final 143.1 ± 0.6 Ma after adjusting for astronomical tuning of stage durations used in GTS2020.

Although the patterns of 2D distribution of points in Figs. 14A.14 and 14A.15 are similar to patterns obtained for Paleozoic periods, including the Devonian, the slightly different procedure (using the unweighted deviations from the spline curve shown in Fig. 14A.15) was used for estimating the 95% confidence limits of the estimated Early Cretaceous stage boundary ages. As pointed out before, unweighted deviations from the spline were used instead of weighted deviations because the 2-sigma values for the dates are probably underestimated. Table 14A.5 contains estimated spline ages for Aptian to Callovian stage bases for which mid-km M-sequence values were available along with their estimated 2-sigma values and the corresponding durations.

In the next three columns of Table 14A.5 durations according to the spline curve are compared with Milanković-based duration estimates. Although the spline ages are probably unbiased estimates of the true ages, the Milanković durations are probably better estimates of stage durations. Much

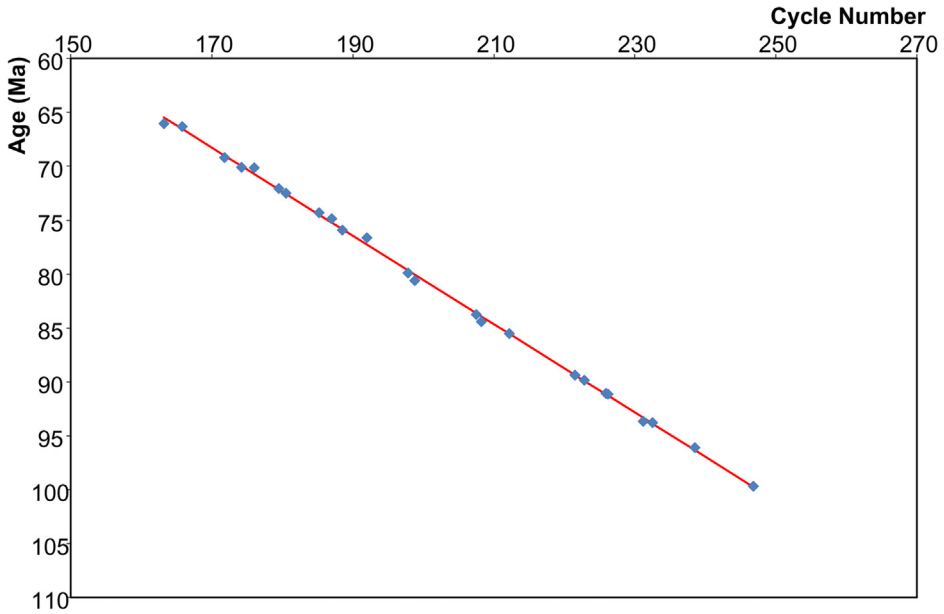

FIGURE 14A.16 Best fitting spline curve for the Late Cretaceous.

of the astronomical tuning of Aptian–Albian time has been based on the Piobbico core drilled into pelagic and hemipelagic strata in the Umbria–Marche Apennines, central Italy. Although the Albian duration using cycles of 12.45 ± 0.5 Myr has been verified by radioisotopic dating, the same is not the case for the Aptian. In GTS2012 the published duration of 13.3 Myr (Huang et al., 2010) is now being contested and a shorter duration of 8.1 ± 0.5 Myr is considered more likely and is adhered to in GTS2020 (see discussions in Ogg, Chapter 5: Geomagnetic Polarity Time Scale, and in Gale et al., Chapter 27: The Cretaceous Period, this book).

Sums of durations from the Albian to the Callovian in Table 14A.5 are 63.4 Myr (spline durations) and 61.5 Myr (M-durations), respectively. The difference between these two sums of durations is 1.9 Myr. Assuming that the Albian and Callovian spline-based age estimates are unbiased, the M-durations can be corrected so that their sum also becomes 63.4 Myr. The resulting ages are shown in the Age-2 column of Table 14A.5. However, when the summation is carried out from the Albian to the Oxfordian (instead of from the Albian to the Callovian), the spline age interval becomes 48.3 Myr and the difference between sums of duration is reduced to 0.84 Myr. Assuming that this estimate is unbiased, the M-durations can be adjusted so that their sum becomes 48.3 Myr as well. The corrected Milanković cycle-durations then can be used to estimate stage base age estimates between the Albian and the Oxfordian. These adjusted estimates together with the previously obtained estimates for the Kimmeridgian, Oxfordian, and Callovian are shown as final age estimates

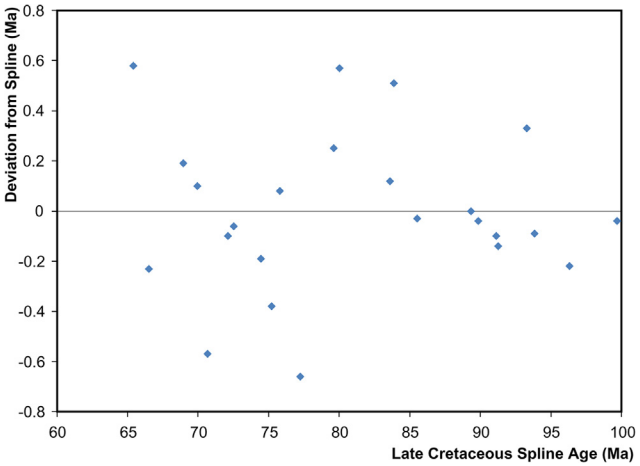

FIGURE 14A.17 Deviations of Late Cretaceous dates (Table 14A.7) as a function of estimated spline values.

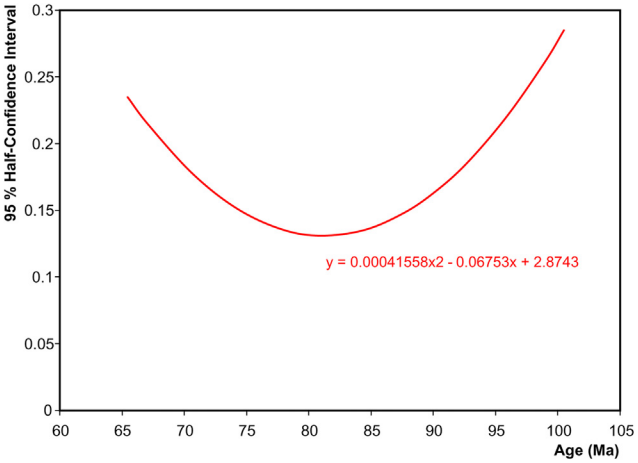

FIGURE 14A.18 Two-sigma values for estimated spline curve of the Late Cretaceous shown in Fig. 14A.6.

TABLE 14A.7 Comparison of Late Cretaceous cycle age determinations with estimated spline age values; $2\sigma'$ represents estimated spline value uncertainty.

Cycles			Spline	
Cycle Value	Age (Ma)	2σ	Age (Ma)	$2\sigma'$
163.18	66.04	0.05	65.46	0.25
165.8	66.31		66.54	0.23
171.8	69.19		69	0.2
174.2	70.08		69.98	0.19
176	70.15		70.72	0.18
180.5	72.5		72.56	0.16
179.5	72.05		72.15	0.17
187	74.85	0.43	75.23	0.14
185.2	74.3		74.49	0.15
188.5	75.92		75.84	0.14
192	76.62		77.28	0.13
197.8	79.9		79.65	0.13
198.8	80.63		80.06	0.13
207.5	83.75		83.63	0.13
208.2	84.43	0.15	83.92	0.13
212.2	85.53	0.35	85.56	0.14
221.5	89.37	0.37	89.37	0.16
222.8	89.86	0.26	89.9	0.16
225.9	91.07	0.28	91.17	0.17
226.2	91.15	0.26	91.29	0.18
231.2	93.67	0.31	93.34	0.2
232.5	93.79	0.26	93.88	0.2
238.5	96.12	0.31	96.34	0.24
246.8	99.7	0.3	99.74	0.29

After final stratigraphic evaluation selected spline uncertainties were slightly revised. See text in Chapter 27, The Cretaceous Period, for further explanation.

in Table 14A.5 along with the original spline-based 2-sigma values and the corresponding revised durations.

Table 14A.6 shows a comparison of the GTS2020 Early Cretaceous age determinations with their estimated spline values. The weights (W) in this table were determined by both the original 2-sigma values of the age determinations and the uncertainties of the mid-km M-sequence magnetic anomaly values. Spline values for the ages of the stage boundaries were modified by accounting for the Milanković cycle-durations. However, this revision that incorporated astronomical-tuned durations for the Berriasian through Barremian stages required another application of the spline-fit procedure to smooth the spreading rates for the M-sequence magnetic anomaly suite (Fig. 5.5 in Chapter 5: Geomagnetic Polarity Time Scale, this volume); and that revised M-sequence age model (Table 5.4 in that chapter) was used for the Middle Jurassic through Early Cretaceous in this book.

TABLE 14A.8 Estimates of the ages of the Late Cretaceous stage boundaries along with their uncertainties, using the spline data in Table 14A.7.

Base of Stage	Age	2-sigma
Danian	66.04	0.05
Maastrichtian	72.15	0.17
Campanian	83.63	0.13
Santonian	85.68	0.14
Coniacian	89.37	0.16
Turonian	93.88	0.2
Cenomanian	100.5	0.14

14A.5.8 Application to the Late Cretaceous

Age determinations for the Late Cretaceous could be correlated with Milanković cycles as shown in Fig. 14A.16 (see Fig. 27.11 in Chapter 27: The Cretaceous Period, this book). A number of dates for which C-sequence and cycle input was available did not have reported 2-sigma values (Table 14A.7) and all dates plotted in Fig. 14A.16 were given equal weights for the spline fitting. The best fitting spline curve is approximately a straight line. Fig. 14A.17 shows the deviations from this spline, which are small. The quadratic 95% half-confidence interval based on these differences is given in Fig. 14A.18 along with its mathematical equation. Spline-curve estimates of the ages of the stage boundaries are listed in Table 14A.8 along with their uncertainties.

The ages and 2-sigma values of base Danian (66.04 ± 0.05 Ma) and base Cenomanian (100.50 ± 0.14 Ma) in Table 14A.7 are not based on the spline curve, because they were determined by other methods as explained in (Chapter 27, The Cretaceous Period, this book). These estimates differ from the spline-curve estimates for the two boundaries, which are 65.43 ± 0.23 and 100.50 ± 0.29 Ma, respectively. The age of base Cenomanian falls slightly outside the range of the Milanković cycle values used for the spline in Fig. 14A.16. However, the quadratic equation of the curve in Fig. 14A.18 was used to derive a spline-based 2-sigma estimate ($=0.29$ Myr) comparable with the 2-sigma values for the other Late Cretaceous stage boundaries of which the ages are also shown in Fig. 27.11 of Chapter 27, The Cretaceous Period (this book).

It is noted that, like in the previous subsection for the Early Cretaceous, the procedure used to estimate the 95%

half-confidence interval is based on the deviations between the input dates and the spline curve, rather than on weights based on the published 2-sigma values of the input dates. The reason for this is that for several of the input dates, the error bars do not intersect the spline curve indicating that, as in the previous subsection, precision of the age determinations was probably overestimated. As discussed in Section 14A.3.2 a similar problem was encountered previously for Paleozoic dates used for GTS2004 and GTS2008. However, for GTS2020 the 2-sigma values of the Paleozoic dates all conform with the 95% half-confidence intervals.

Table 14A.7 shows a comparison of the GTS2020 Late Cretaceous cycle age determinations with their estimated spline values. Weights for the spline fitting were set equal to 1 in this application. Spline values for the ages of the stage boundaries were modified by accounting for the Milanković-durations. Finalized stage boundary ages, combining cycle, radiometric, and C-sequence data are in Table 14A.8.

Bibliography

Agterberg, F.P., 1974, *Geomathematics*. Amsterdam: Elsevier, p. 596.

Agterberg, F.P., 1988, Quality of time scales – a statistical appraisal. *In* Merriam, D.F. (ed), *Current Trends in Geomathematics*. New York: Plenum, 57–103.

Agterberg, F.P., 1994, Estimation of the Mesozoic geological time scale. *Mathematical Geology*, **26**: 857–876.

Agterberg, F.P., 2002, Construction of numerical geological time scales. *Terra Nostra*, **04/2002**: 227–232.

Agterberg, F.P., 2004, Appendix 3: Geomathematics. *In* Gradstein, F.M., Ogg, J.G., and Smith, A.,G. (eds), *A Geologic Time Scale 2004*. Cambridge University Press, 485–486.

Cantrell, C.A., 2008, Technical note: review of methods for linear least-squares fitting of data and application to atmospheric chemistry problems. *Atmospheric Chemistry and Physics*, **8**: 5477–5487.

Chambers, J.M., and Hastie, T.J., 1992, *Statistical Models in S*. London: Wadsworth and Brooks/Cole, p. 608.

Cooper, R.A., 1999, The Ordovician Time Scale – calibration of graptolite and conodont zones. *Acta Universitatis Carolinae Geologica*, **43** (1/2), 1–4.

Cox, A.V., and Dalrymple, G.B., 1967, Statistical analysis of geomagnetic reversal data and the precision of potassium-argon dating. *Journal of Geophysical Research*, **72** (10), 2603–2614A.

De Vleeschouwer, D., and Parnell, A.C., 2014, Reducing th0me-scale uncertainty for the Devonian by integrating astrochronology and Bayesian statistics. *Geology*, **42** (6), 491–494.

Getis, A., and Ord, J.K., 1992, The analysis of spatial association by use of distance statistics. *Geographical Analysis*, **24** (3), 189–206.

Gradstein, F.M., Agterberg, F.P., Ogg, J.G., Hardenbol, J., van Veen, P., Thierry, T., et al., 1994, A Mesozoic time scale. *Journal of Geophysical Research*, **99** (B12), 24051–24074.

Gradstein, F.M., Agterberg, F.P., Ogg, J.G., Hardenbol, J., van Veen, P., Thierry, T., et al., 1995, A Triassic, Jurassic and Cretaceous time scale. *In* Berggren, W.A., Kent, D.V., Aubry, M.-P., and Hardenbol, J. (eds), Geochronology, Time Scales and Global Stratigraphic Correlations: A Unified Temporal Framework for a Historical Geology. *Society for Sedimentary Geology Special Publication,* **54**: 95–128.

Gradstein, F.M., Ogg, J.G., and Smith, A.G. (eds), 2004. A Geologic Time Scale 2004. Cambridge University Press. Cambridge.

Gradstein, F.M., Ogg, J.G., Schmitz, M.D., and Ogg, G.M. (eds), 2012. The Geologic Time Scale 2012. Elsevier. Amsterdam.

Haslett, J., and Parnell, A., 2008, A simple monotone process with application to radiocarbon-dated depth chronologies. *Applied Statistics*, **57** (4), 399–418.

Hastie, T.J., and Tibshirani, R.J., 1990, *Generalized Adaptive Models*. London: Chapman and Hall, p. 328.

Harland, W.B., Cox, A.V., Llewellyn, P.G., Pickton, C.A.G., Smith, A. G., and Walters, R., 1982, *A Geologic Time Scale*. Cambridge: Cambridge University Press, p. 131.

Harland, W.B., Armstrong, R.L., Cox, A.V., Craig, L.A., Smith, A.G., and Smith, D.G., 1990, *A Geologic Time Scale 1989*. Cambridge: Cambridge University Press, p. 263.

Howarth, R.J., and McArthur, J.M., 1997, Statistics for Strontium isotope stratigraphy: a robust LOWESS fit to the marine Sr-isotope curve for0 t0 206 Ma, with look-up table for derivation of numeric age. *Journal of Geology*, **105**: 441–456.

Huang, C., Hinnov, L., Fischer, A.G., Grippo, A., and Herbert, T., 2010, Astronomical tuning of the Aptian Stage from Italian reference sections. *Geology*, **38**: 899–902.

Kent, D.V., and Gradstein, F.M., 1985, A Cretaceous and Jurassic geochronology. *Geological Society of America Bulletin*, **96**: 1419–1427.

Kent, D.V., and Gradstein, F.M., 1986, A Jurassic to Recent geochronology. *In* Vogt, P.R., and Tucholke, B.E. (eds), *The Geology of North America. Vol. M, The Western North Atlantic Region*. Boulder, CO: Geological Society of America, 45–50.

Lybanon, M., 1984, A better least-squares method when both variables have uncertainties. *American Journal of Physics*, **52**: 22–26.

McKerrow, W.S., Lambert, R.S.J., and Cocks, L.R.M., 1985, The Ordovician, Silurian and Devonian Periods. *In* Snelling, N.J. (ed), The Chronology of the Geological Record. *Geological Society of London, Memoir,* **10**: 73–80.

Obradovich, J.D., 1993. A Cretaceous time scale. *In* Caldwell, W.G.E., and Kaufman, E.G., (eds), Evolution of the Western Interior Basin. *Geological Association of Canada Special Paper*, **39**: 379–396.

Odin, G.S., 1994, Geologic Time Scale 1994. *Comptes rendus de l'Académie des Science de Paris, série II*, **318**: 59–71.

Ovtcharova, M., Goudemand, N., Hammer, Ø., Guodun, K., Cordey, F., Galfetti, T., et al., 2015, Developing a strategy for accurate definition of a geological boundary through radio-isotopic and Biochronological dating: the Early-Middle Triassic boundary (South China). *Earth-Science Reviews*, **146**: 65–76.

Pálfy, J., Smith, P.L., and Mortensen, J.K., 2000, A U-Pb and $^{40}Ar/^{39}Ar$ time scale for the Jurassic. *Canadian Journal of Earth Sciences*, **37**: 923–944.

Press, W.H., Teukolsky, S.A., Vettering, W.T., and Flannery, B.R., 1992, *Numerical Recipes in FORTRAN*. Cambridge: Cambridge University Press, p. 963.

Ripley, B.D., and Thompson, M., 1987, Regression techniques for the detection of analytical bias. *Analyst*, **112**: 377–383.

Wahba, G., 1985, A comparison of GCV and GNL for choosing the smoothing parameters in the generalized spline smoothing problem. *Annals of Statistics*, **4**: 1378–1402.

Wang, Y., 2011, *121. Smoothing Splines. Methods and Applications, Monographs on Statistics and Applied Probability*. Boca Raton, FL: CRC Press, p. 370.

SubChapter 14B

Global Composite Sections and Constrained Optimization

P. Sadler

Abstract

Stratigraphic information from a wide array of locations must be combined to mitigate incompleteness in local stratigraphic records, to capture the geographic distribution and diachronism of index taxon ranges, to amalgamate provincial biotic successions in different environments, and to encompass enough reliably dated events. Constrained optimization seeks a single succession of events to which all local sequences can be fit with minimum net adjustment of locally observed event horizons. This optimized composite sequence is constrained to honor any immutable superpositional relationships between event pairs established at local sections, such as taxon cooccurrences. The optimization proceeds by iterative improvement to find the best fit order of events. An objective function is chosen according to the desired properties of the emergent composite. It sums misfits between feasible composites and all the real local sections. Two nested optimizations are performed. The outer optimization finds the fittest global sequence of events, an ordinal composite sequence with no differentiation of interevent spacing. The inner optimization finds the most parsimonious adjustment of local event horizons to match the global sequence. The optimal spacing of events across all adjusted local sequences guides conversion of the ordinal composite to a scaled composite section on which age is then interpolated between dated events by curve-fitting techniques. The smoothing factor in LOWESS regression, for example, highlights the question of how closely the regression should track individual dated events or run more smoothly through the ensemble. This is the last in a series of assumptions and uncertainties that accumulate with each step in the time scale building process. Ideally, weaker assumptions enter at later stages. In particular, event spacing requires more questionable assumptions than event ordering.

14B.1 The geologic time scale challenge

One of the necessary first steps toward a geologic time scale (GTS) places a suite of fossil events in global order of occurrence, as determined from numerous local stratigraphic sections. Taxon originations and extinctions in the global succession of fossil organisms account for the majority these events (Fig. 14B.1). There order must be inferred from local appearances and extirpations. Other events to be placed in the time line include geomagnetic field reversals, rapid stable isotopic changes, and radioisotopic-dated ashfalls. The numerous biotic events cluster unevenly, recording rare intervals of mass extinction or rapid innovation. Historically, these clusters were used to divide the biotic succession into a series of named stratigraphic units. This step established a relative time scale and a vocabulary of named units for coarse global correlation (Berry, 1968). The final steps interpolate ages from the relatively few dated events in the succession to the conventional unit boundaries and key events in geologic history. Thus rate estimates become possible for past changes in the Earth's environment, landscape, and life. We shall explore several factors that render these steps particularly challenging: the huge volume of information, its geographic variability, its local incompleteness, and the relative paucity of dated events.

14B.1.1 Scope of the task

The volume of stratigraphic data relevant to the GTS can overwhelm even expert individuals. Consider the Ordovician and Silurian Periods. Successions of rich graptolite and conodont faunas allow local recognition of finely resolved biozones in basin and shelf environments. The continual compilation of local range charts for the early Paleozoic record of these two clades, since GTS2004 (Gradstein et al., 2004; Sadler et al., 2009, 2011), has now accrued records for 2651 graptolite taxa from 836 locations and 2196 conodont taxa from 1056 locations. The number of locally recorded taxon range ends and associated environmental change events is now 33,531 and 40,959, respectively, for these two databases (Fig. 14B.2)—a superb evidence base for reconstructing global biotic succession, but one requiring sophisticated numerical methods and computer assistance.

Dell et al. (1992) recognized that stratigraphic sequencing and correlation is a strongly "NP-hard" problem. This class of optimization task includes the classic traveling salesman problem. Computation time increases exponentially, or faster (Kemple et al., 1995), with the number of sections and taxa. It is not feasible to undertake an exhaustive examination of all possible sequences of events and yet the remedy is not to reduce the size of the database. Fortunately, several efficient search algorithms have been developed for this class of problem. To take advantage of one of these methods, simulated annealing, we map the GTS problem into the traveling salesman problem (Kemple et al., 1995). Cities on the salesman's route become events, geologic events; the number of them determines the scope of the problem. Distances between cities become local range-end adjustments; the sum to be minimized. The shortest route that visits every city once and only once emerges as the optimal geologic time line.

14B.1.2 Incomplete parochial records

It is generally not feasible to build a global GTS upon a few key stratigraphic sections. Most sections yield an incomplete sedimentary record (Sadler, 1981) and a less complete record of the ranges of fossil species (Marshall, 2010).

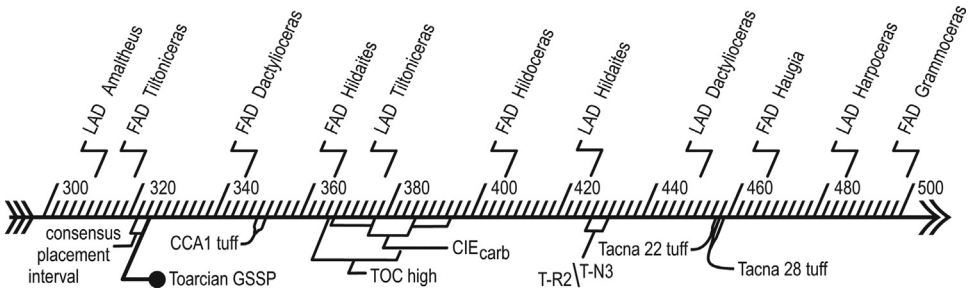

FIGURE 14B.1 Example components from a 200-event segment of an early Jurassic ammonite time line fitted to 10,033 local event records for 490 genera in 354 sections, worldwide. Events are uniformly spaced; taxon range-end events shown here above the line, with a few examples labeled. Other example events (labeled below the line): traceable ashfall tuffs (some dated); a stage-boundary GSSP; a consensus interval that represents the overlap of locally inferred stage boundary uncertainties; a magnetostratigraphic polarity reversal (T-R2\T-N3) interval; a peak in TOC; and a CIE consensus interval, with the onset and decline separated. *CIE*, Carbon isotopic excursion; *TOC*, total organic carbon.

Sediment accumulation is intermittent; organisms are patchy distributed; their preservation is uncertain and fossil collecting is imperfect. As a consequence, the sequence of recorded taxon appearances and extirpations varies from section to section, even within a single province. A suite of sections is desirable to compensate for many sources of incompleteness. Some sections enjoy rich preservation and closely spaced sampling but are inevitably restricted to a tiny part of a dynamic environmental mosaic. They are not globally representative. Many regions must be interrogated to capture the geographic scope and diachronism of taxon range limits. This inclusive approach is typically necessary to incorporate those few and disparate local sections that include dated events. Such sections must be incorporated whether or not they yield a rich fossil record.

There is a strong statistical argument in favor of composite sequences (Strauss and Sadler, 1989; Glazner and Sadler, 2016). For a uniform random distribution of n local samples within a local taxon range, the expected full taxon range $\overline{R}$ becomes increasingly larger than the observed range R_{obs} as n decreases (Fig. 14B.3).

$$\overline{R} = R_{obs}\left(\frac{n+1}{n-1}\right) \tag{14B.1}$$

Note that the denominator $(n-1)$ is the number of gaps between the finds that establish the observed range. The numerator $(n+1)$ adds two more gaps, one between the true appearance and the oldest find and the second between the youngest find and the true extirpation.

Eq. (14B.1) has discouraging implications for the correlation of range-end events. Because the collection success (n) varies between sections and taxa, it is unlikely that the sequence of reported range ends will match even between nearby sections. Truly coincident range ends are likely to be separated in the preserved record. False range-end coincidences will be created at richly fossiliferous levels and at

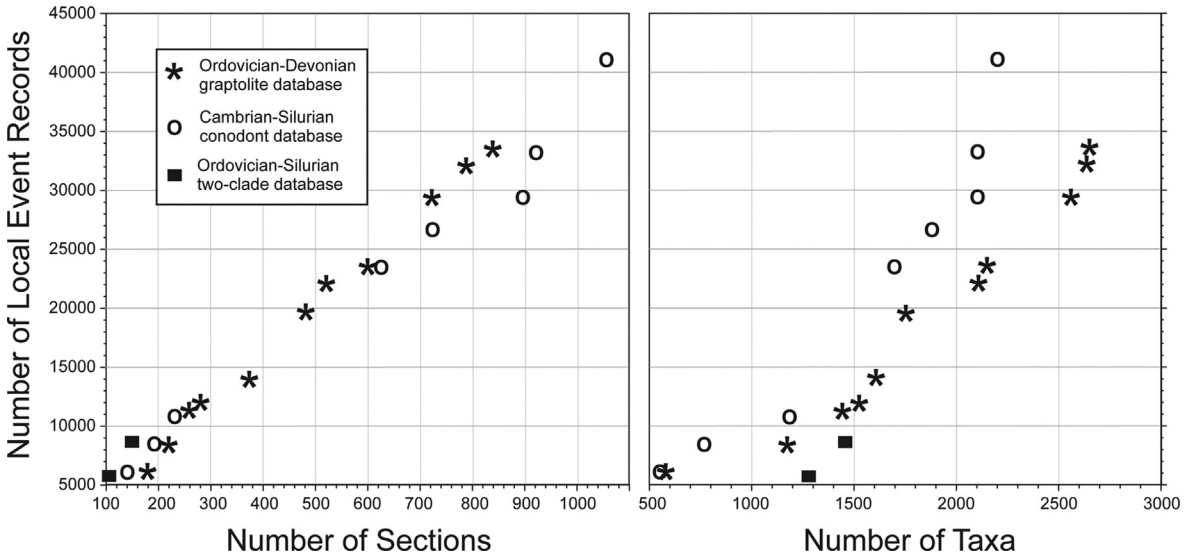

FIGURE 14B.2 Growth of graptolite and conodont databases compiled in support of the Ordovician and Silurian composite sections. The two-clade database is limited to sections from which taxa of both clades have been identified.

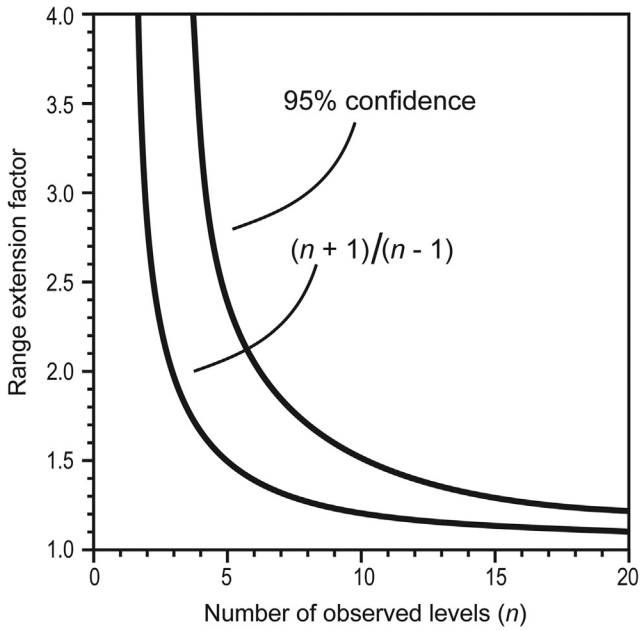

FIGURE 14B.3 Extension factors to correct observed ranges drawn through n random samples from the true range. Lower curve: the mean duration of true taxon ranges, expressed as a multiple of the observed range, that could be expected to yield the observed span of n occurrence levels. Upper curve: greater extension corrections needed to capture 95% of true ranges that could have yielded the n random finds.

hiatuses. The shortfall of the observed range duration may be greater than Eq. (14B.1) suggests, because fossils are not expected to be found uniformly with the taxon range. The abundance of a taxon is likely low near its first appearance and likely falls again near extirpation.

For a local taxon range based upon only a single sample, the expected range is unconstrained—the denominator in Eq. (14B.1) goes to zero. How do we instinctively determine whether a single local find indicates an abundant short-ranged taxon or a rare long-ranged taxon? We compare many localities. A composite section achieves this rigorously. In compensation for some uncertainties in correlation, the composite sequence increases n and with it our confidence in the sequence of range ends. With local information about the order and overlap of taxon ranges, various numerical methods are available to identify most likely sequences of range-end events (Tipper, 1988; Guex, 1991; Sadler, 2004; for summaries). Radioisotopic dates, paleomagnetic records, and stable isotope time series help narrow further the likely true sequences (Sadler, 2006, 2010).

14B.1.3 Optimized global composite sections

Early biostratigraphy and GTSs progressed (Berry, 1968) by combining information from multiple locations to improve resolving power and fidelity. A stack of successive biozones, derived from observations of the biotic succession in several stratigraphic sections, provides a composite ordinal scale into which dated events can be inserted subjectively. Interpolation on an ordinal scale is necessarily coarse, however, and the process becomes less satisfactory as the number and geographic scope of dated events increases, accelerated by the GSSP (Global Boundary Stratotype Section and Point) convention. It is preferable to build a composite section of taxon ranges and other events without the a priori inclusion of zone boundaries. Instead, zone boundaries can be identified subsequently in the emergent composite as they would be located in a local, but less complete, section.

One of the first numerically approaches to composite stratigraphic information at the taxon range-end scale was Shaw's (1964) graphic correlation (Mann and Lane, 1995; Shaw, 1995). Using a line of correlation (LOC) in a manner comparable to linear regression on two-axis graphs, Shaw built a scaled composite section by projecting new information, one section at a time, into the thickness scale of the best of the real local sections. The underlying assumption was that locally preserved and collected taxon ranges tend to be shorter than true regional or global ranges. Shaw's method has been widely adopted to compile regional and global composite sequences for graptolite ranges (e.g., Cooper and Lindholm, 1990; Grubb and Finney, 1995) and conodont ranges (e.g., Sweet, 1984, 1995, 2005; Kaufmann, 2006; Kleffner and Barrick, 2011). This iterative, two-dimensional approach quickly becomes unwieldy when dealing with dozens of sections, but some efficiency has been regained with computer-assisted versions (Hood, 1986; Fan and Zhang, 2000).

Several programs have been developed that build composite sections from larger data sets than is feasible by graphic correlation (Sadler et al., 2014). They treat information from all sections at once and differ according to the data they select and the question answered. Graphic correlation uses the local sequence and spacing of events and seeks, for each taxon, the earliest of the local first appearances and latest of the last appearances. Edwards's (1978) "no-space graphs" and the RASC (Ranking and Scaling) program (Agterberg and Nel, 1982; Agterberg and Gradstein, 1999) seek the sequence before attempting spacing, because that eliminates the complication of locally variable accumulation rates. Like graphic correlation, the no-space graphs seek the succession of extreme range end events—the biologic history. RASC uses locally observed pairwise sequencing of events and builds a composite succession from the most frequently observed of the two possible pairwise orders. In effect, it asks what the next real section will most likely yield. Other programs prefer to trust only those local observations that cannot be artifacts of underrepresented local ranges. The methods of unitary association (Guex, 1977, 1991; Savary and Guex, 1991; Monnet et al., 2011) and conjunction (Alroy, 1992) use observed

coexistences. Appearance event ordination (Alroy, 1994) uses taxon pairs for which the first appearance of one precedes the last appearance of the other.

The core of the CONOP (constrained optimization) program (Kemple et al., 1989, 1995; Sadler et al., 2003) is a search algorithm. Its parameters may be set to mimic the logic and preferences of the programs mentioned previously. CONOP extends graphic correlation from two to as many dimensions as there are local sections (Kemple et al., 1995), thus, eliminating worries about the order in which sections are added. The preferred CONOP settings for time scale calibration effectively measure stratigraphic distance in the manner of no-space graphs and use the logic of unitary association and appearance event ordination to add constraints. The program has been successfully applied to biostratigraphic data from the Neoproterozoic (Riedman and Sadler, 2018) and Paleozoic (e.g., Hints et al., 2011; Rubel et al., 2006; Sadler and Sabado, 2009; Sadler et al., 2011; Shen et al., 2011; Webster et al., 2003), to the Cenozoic Era (e.g., Cooper et al., 2001; Cody et al., 2008; Daneshian et al., 2017). CONOP uses only taxon range ends.

14B.1.4 Two nested optimizations

If the fitness of a composite sequence is judged solely by how few taxon coexistences it implies, beyond those known from the local fossil records, only a single optimization is needed to minimize the excess implied coexistences. If fitness is judged by comparison with all local orderings of events, whether or not these could be an artifact of underrepresented ranges, optimization must be performed on two nested levels (Kemple et al., 1995). An outer optimization examines the relative fitness of numerous possible global sequences of events. The inner optimization returns the most parsimonious adjustment of observed event levels that brings each local section into alignment with the composite sequence. The outer (global) optimization is concerned only with the order of events, not their spacing. The inner (local) optimization arranges the record of these events on each local thickness or sampling scale and lays the foundation for subsequently scaling the intervals between events in a global composite section. Only the inner optimization needs to consider the complication that two or more events seem to occur at the same time; that is, they are placed at the same local stratigraphic level and any interval separating them is locally irresolvable (zero spacing).

14B.2 Constrained optimization of a composite section

CONOP solves problems by discarding illegitimate solutions (constraint), while exploring the remaining solution space for one that best fits the data (optimization). For global GTSs the best solution is a single succession of events to which all local sequences can be matched with a minimum net adjustment of observed event levels, up- or downsection. This section explains the process in terms of five successive decisions: (1) assign the stratigraphic events to different classes according to permitted adjustments; (2) identify constraints in event ordering that the composite section must honor; (3) determine the complexity that the LOC may assume; (4) formulate a measure of misfit between the composite and local sections; and (5) choose a search procedure that effectively reaches very good solutions (Kemple et al., 1995). Simplifying assumptions are necessary but are incorporated as late as possible in the succession of decisions.

14B.2.1 Data classes

The wide variety of events that might be incorporated in a geologic time line reduces to a few simple categories according to their stratigraphic fidelity (Sadler and Cervato, 2011); that is, the associated uncertainty in local position that determines their reasonable adjustment when fitting the local sequence to a global composite succession. The three most useful classes share some properties with jacks, clamps, and nails (Fig. 14B.4). By using these workshop names for the data classes, we can more readily appreciate how a locally observed sequence limits our degrees of freedom in the search for the best fit global sequence of events. The optimal sequence becomes the one that avoids pulling any nails and requires the least effort in adjusting all the jacks and clamps.

Taxon ranges dominate the available information. They are intervals between local first and last occurrences. The local ranges might approximate the duration of the true global range but are more likely shorter. They belong to the stretch-to-fit data class. The composite taxon range spans the interval where the taxon is known *anywhere*. Imagine the base (oldest find) and top (youngest find) of the local range as separated by a *jack*. At the cost of some effort the ends of the range may be jacked farther apart, increasing the local duration. The optimal global sequence minimizes the physical effort represented by all the jacks as they stretch local ranges to fit the global succession of range ends. Local first appearances may only adjust downsection and last appearances upsection. This is the operating principle of graphic correlation. Jacks may stretch a range end to the limit of the local section. No greater effort is then required to fit placements far beyond the age of the local section limit. In effect, range ends that coincide with the limits of a section do not limit the extent of the global composite range.

In the physical analogy, another class of data would be represented by a *clamp*. This class shrinks to fit. It includes uncertainty intervals that overestimate true

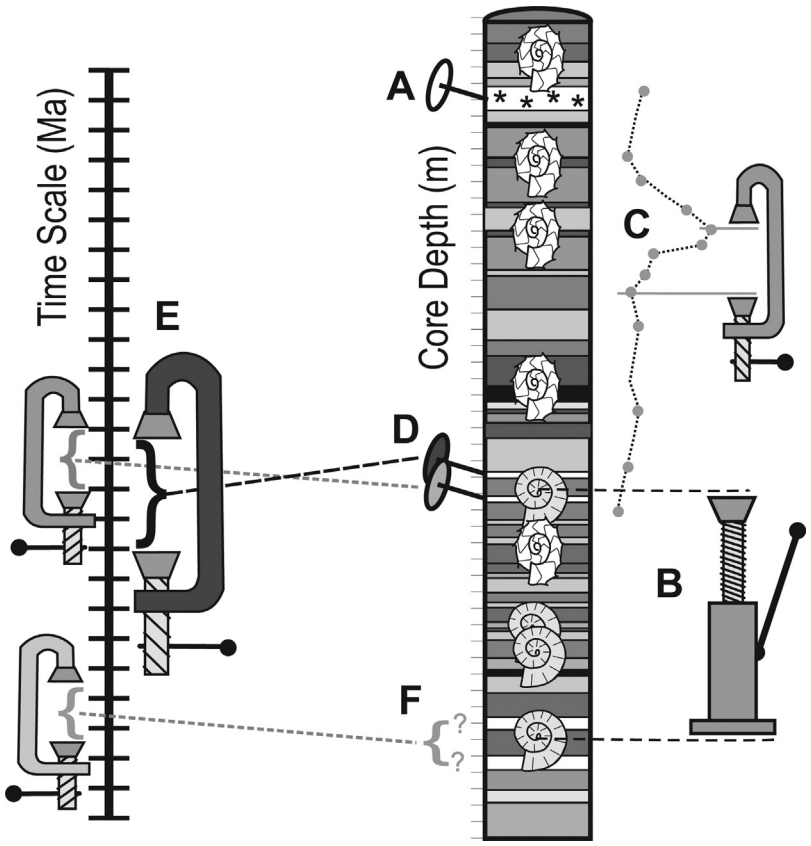

FIGURE 14B.4 Examples for three classes of uncertainty in stratigraphic information—"nails, jacks, and clamps." (A) Uniquely fingerprinted marker bed: a "nail" point that may not be adjusted. (B) Observed local taxon range that likely underrepresents the global range; a "jack" interval that may stretch to fit the composite sequence of events. (C) A conservative uncertainty interval on the position of steepest change in a stable isotope anomaly; a "clamp" interval that may shrink to fit. (D) The local "nailed" position of two samples for radioisotopic dating. (E) The analytical uncertainty of the ages of the same samples now "clamped" onto an age scale shared with other dated events. (F) "Clamp" expresses ambiguity in the location of a dated sample. For (D) and (E) the sampled positions indicate that the analytical mean ages are out of order; the corresponding clamp intervals overlap and will shrink to fit the superpositional evidence of order. The local ranges of the two fossil taxa overlap; the composite sequence must be constrained to include this relationship.

duration and, at the cost of some effort, may be clamped down. For example, the rock intervals between adjacent samples that record normal and reversed remanent magnetization are such intervals for geomagnetic chron boundaries. We use the same class for carbon isotope anomalies (Sadler, 2012), entering their maximum reasonable extent in local sections. All the local uncertainties are assumed to overlap in time and the composite placement of the anomaly lies within these uncertainty limits *everywhere*. In contrast to jacks that may stretch beyond the local section, the shrinkage of a clamp is limited to closure. Where uncertainty vanishes the clamp becomes a nail—the event class that may not be adjusted up- or downsection. Each local occurrence of a chemically fingerprinted ashfall behaves a *nail*. If the local placement is in conflict with better constrained events, the identification is in question and the nail must be removed.

A dated ash bed usually has the property of a nail in the section where it was sampled, but a clamp when recorded in an age-scaled "section" with other dated events. The 2-sigma analytical uncertainty, which is used to scale the width of the clamp, may shrink in response to superpositional relationships with other events and dates. If the reported location of the sampled ash bed is ambiguous, it too may be treated as a "shrink-to-fit" clamp. In earlier GTS volumes, dated Ordovician and Silurian K-bentonites were identified by their mean ages and treated as nails. With increasing numbers of dated events, some of the 2-sigma intervals overlap. To recognize that mean ages might not record the true order of such events, it has become safer to assign these dated events to the clamp category (Fig. 14B.5).

Many local taxon ranges stretch to fit their final composite extent as guided by multiple interactions with other range-end events. Only a few of the 2-sigma uncertainty intervals on radioisotopic dates shrink to fit the composite sequence. This data class is not numerous, and opportunity for shrinkage is limited to the age-scaled section.

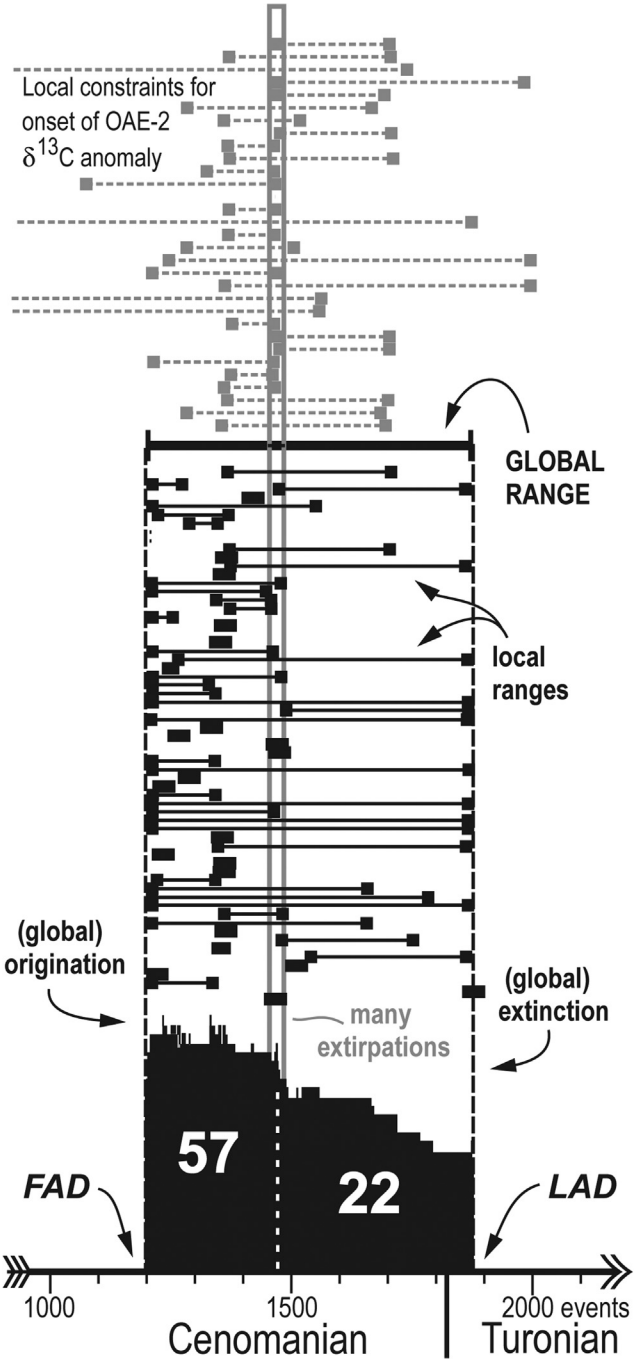

FIGURE 14B.5 Part of a best fit ordinal time line of 3275 mid-Cretaceous events from 489 localities. Gray rectangle: global consensus interval is the overlap of local uncertainty intervals (shrink-to-fit "clamps") for the onset of a carbon isotope anomaly. Black bars: global composite range encompasses all local ranges for *Rotalipora cushmani* (stretch-to-fit "jacks"). Black histogram sums the number of local ranges that support global composite range.

Imprecise dates from earlier GTS projects tend to shrink significantly within their large published uncertainties, without distorting the calibration regressions. This shrinkage is often very asymmetric. The published mean age may be left outside the shrunken uncertainty interval, indicating that the mean age was misleading. As shrink-to-fit clamps, these old dates do no harm to the composite sequence. Depending on the regression technique, however, the safest practice may leave them out of the set of tie points for age calibration.

14B.2.2 Constraints

Some local ordering relationships are immutable in the sense that they cannot be an artifact of incomplete preservation. They are constraints in the sense that the composite section must reproduce them. The first appearance of a taxon must precede its last. Similarly, if two taxa are proven to coexist, anywhere, both first occurrences must be placed in the composite sequence before either last occurrence. This limits the number of feasible global sequences of events that need to be tested for fitness. It follows that even a very taxon-poor local section would place a significant constraint on the global sequence, if it were the only evidence for a coexisting taxon pair—perhaps two taxa that rarely inhabit the same environment. Even isolated slabs in a museum collection may serve this purpose (Webster et al., 2003).

Pairwise ordering constraints can best be summarized using the physical analogs, jack, clamp, and nail. Wherever an event that may only be adjusted downsection, if at all, has been reported below an event that adjusts upsection only (younger limit of a jack, or older limit of a clamp), or not at all (the nail category), that pairwise ordering is a constraint that cannot be an artifact of incomplete preservation. The same is true for an event that may only be adjusted upsection and has been observed anywhere above one that adjusts downsection only (older limit of a jack interval, or younger limit of a clamp) or one that may not adjust (a nail). Note that this logic assumes that reworked fossils have been culled from the input data. If not, locally reported ranges must be allowed to shrink from the top, but with a much smaller probability than stretching to fit (Cody et al., 2008).

We also assume that taxa have been identified correctly. Such mistakes do occur, or course. Some are first identified by gaps and outliers in the emergent composite ranges. Thus the compositing process serves as one source of quality control (Sadler, 2010).

14B.2.3 Line of correlation

The LOC by which local information is projected from a local section into the composite sequence during graphic correlation must have a positive slope; age does not reverse. Shaw (1964) initially favored linear regression. Here (Fig. 14B.6), we adopt the opposite end-member in permissible complexity, a piecewise linear regression with no limit on the degree of segmentation and permissive of segments that parallel the axes and imply hiatuses in the local sections

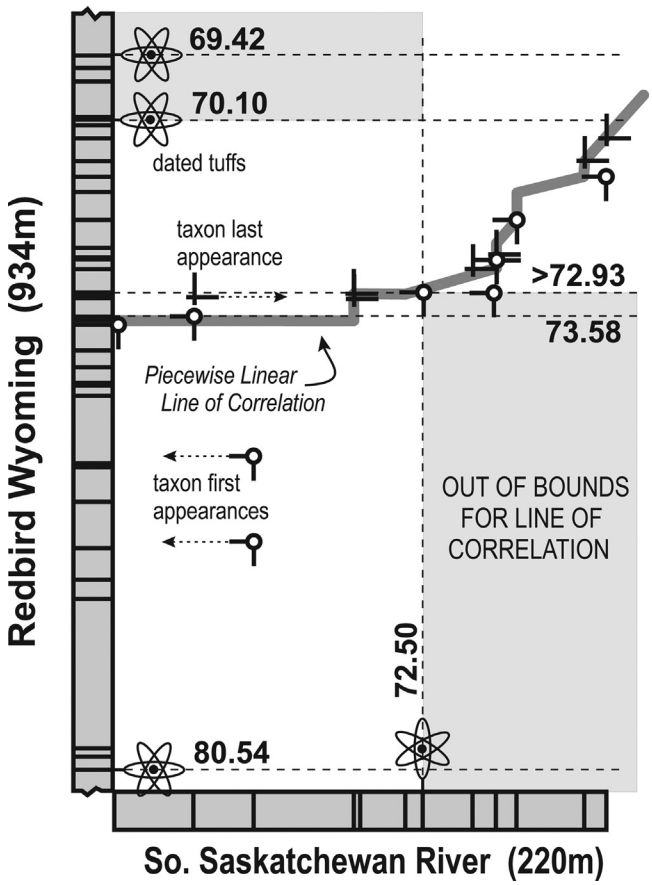

FIGURE 14B.6 Graphic line of correlation (LOC) between two Cretaceous ammonite-bearing sections with radioisotopic dates and a dated paleomagnetic interval. Dated events divide graphic plot into rectangles; piecewise linear LOC must cross rectangle boundaries in order of ages, leaving some rectangles (*pale gray fill*) impossible for LOC to enter. Best fit LOC (*thick gray line*) is projected into this 2-section plane from a global, 561-section, constrained optimization of 1213 ammonite taxon ranges, and 162 other events. Circle and cross symbols are coordinates of first- and last-appearance levels, respectively, for shared ammonite taxa; the attached bars indicate permitted directions of range extension to fit LOC. Most parsimonious range extensions (*dashed arrows*) all impact the less richly fossiliferous South Saskatchewan River section.

(MacLeod and Sadler, 1995). In graphic correlation the LOC is manipulated by the stratigrapher on a series of two-dimensional graphs. In CONOP the LOC exists in $j+1$ dimensions—the number of local sections (j) plus the composite sequence—and is managed by the objective function (Eq. 14B.2). Full piecewise complexity is facilitated by omitting any smoothing term in the objective function (Kemple et al., 1995). Without a smoothing term the objective function effectively optimizes only the global order of events, not their spacing. It develops a composite *sequence*. The differential spacing of events necessary for a composite *section* or proxy time scale is determined with additional assumptions, *after* an optimal sequence is determined without them (Sadler et al., 2009). Simplifying assumptions about local rate and age need not compromise optimization of the order of events.

14B.2.4 Objective function

The optimal composite sequence minimizes the objective function (Eq. 14B.2), which sums the misfit of trial composite sequences relative to all the real local sections. Symbols $\boldsymbol{a}$ and $\boldsymbol{b}$ are the locally observed downsection and upsection limits of an interval. They have been adjusted to α and β, respectively, by stretching or shrinking depending on data class. The absolute sizes of the adjustments are considered ($|\boldsymbol{a}-\alpha|$) and ($|\beta-\boldsymbol{b}|$); stretch-to-fit and shrink-to-fit adjustments do not compensate for one another.

$$F=\left(\sum_i\sum_j\left[w_{1ij}\left(|\boldsymbol{a}_{ij}-\alpha_{ij}|\right)+w_{2ij}\left(|\beta_{ij}-\boldsymbol{b}_{ij}|\right)\right]\right)+K\left(N^c_{\text{comp}}-N^c_{\text{obs}}\right) \tag{14B.2}$$

Subscripts i and j indicate events and sections, respectively. Weights w_{1ij} and w_{2ij} allow differential emphasis on every locally observed event but are all usually set to 1.00 by default when a composite sequence is first optimized. The summation terms mean that more commonly occurring events inherently carry more weight than rare events.

The dual summation in the first term ceases to grow when the end of a stretch-to-fit interval is "jacked" beyond the limits of a local section. A stretched range is likely to overlap with increasing numbers of other taxon ranges, however, and if any of these coexistences are not observed elsewhere, the difference term without ij subscripts ($N^c_{\text{comp}}-N^c_{\text{obs}}$) discourages further stretching. This second term in the objective function subtracts from the number of coexisting taxon pairs implied by the composite sequence N^c_{comp} only those confirmed by overlapping ranges in at least one local section N^c_{obs}. The impact of this term on the total misfit is adjusted by the weight K, usually between 0.1 and 0.001.

Although the numerous possible weights w_{1ij} and w_{2ij} are typically all set to 1.00 for time scale purposes, the measurement scale for ($|\boldsymbol{a}-\alpha|$) and ($|\beta-\boldsymbol{b}|$) does determine which sections most influence the outcome. Traditional graphic correlation uses rock thickness (penalty = "interval" in CONOP configuration file) and, thus, favors sequences seen in thicker sections. To favor richer and more finely sampled sections, we measure the size of adjustments by their span of event levels (penalty = "level").

14B.2.5 Simulated annealing

Of the various search algorithms developed for NP-hard problems, CONOP adopts the simulated annealing heuristic (Kirkpatrick et al., 1983). It manages a trial-and-error process analogous to tracking the free energy changes in an attempt to grow a perfect crystal by slow cooling from a molten state. The search begins with a sequence of events π that merely satisfies the coexistence constraints (Fig. 14B.7A): first occurrences are placed in random order at the start of the sequence

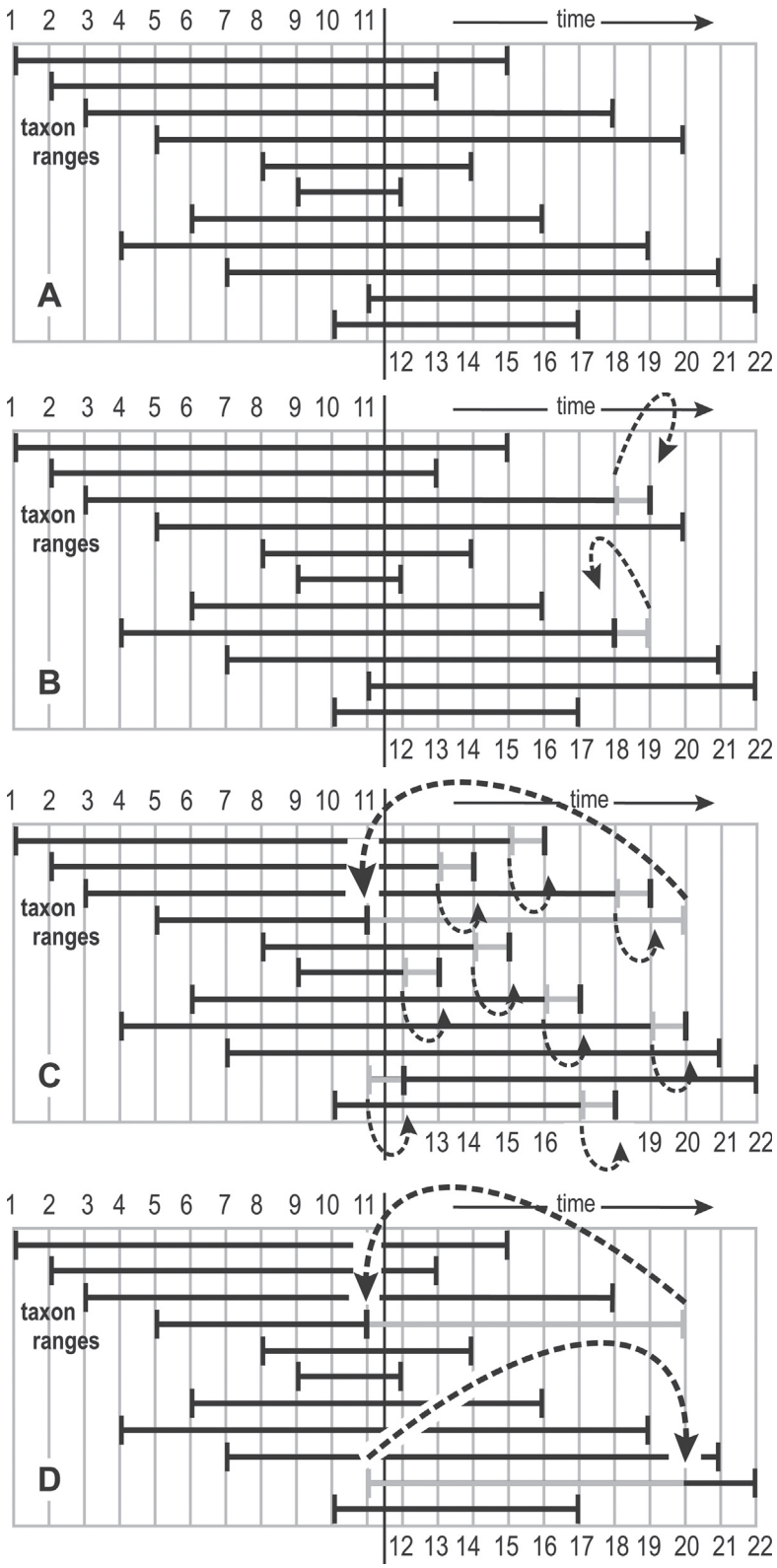

FIGURE 14B.7 Sequence permutation by CONOP: (A) initial configuration; all taxa coexist; all coexistence constraints satisfied; (B) random neighboring events swap positions; small changes, best near end of search; (C) random event moves to new random position; all intervening events shift one position; efficient throughout search; and (D) random event pair swaps positions; large changes, best near beginning of search. *CONOP*, Constrained optimization.

and last occurrences at random at the end. Events of other classes are initially placed in the mid-section and internally ordered according to pairwise constraints. Each trial then moves a randomly chosen event to a new random position (Fig. 14B.7C). Moves that violate any constraint are immediately rejected. Moves that reduce or do not alter the misfit are always retained. Moves that increase the objective function ($\delta F > 0$), making the developing solution temporarily less fit, are evaluated by a Boltzmann-like term (Eq. 14B.3), which yields the probability P_T of accepting the new sequence (π) in spite of some loss of fitness.

$$P_T(\pi) = \begin{cases} 1, & \delta F \le 0 \\ e^{-(\delta F/T)}, & \delta F > 0 \end{cases} \qquad (14B.3)$$

The temperature term T in the exponent prevents the optimization from becoming trapped in a local minimum. T is reduced stepwise by a factor 0.95 during the search and with it the likelihood of accepting a move that worsens the fit of the composite sequence to the local sections (Eq. 14B.2). Initially, T is set large enough that at least half of all moves would be accepted. As T decreases, acceptance becomes more dependent on δF until, at the end of the search, T is close enough to zero that only improvements in fit are accepted.

The cooling rate determines the number of trial moves attempted at each cooling step. For small data sets, this number may be fixed at a few thousand (Kemple et al., 1995). For the huge data sets used in the time scale challenge, an adaptive simulated annealing algorithm determines its own cooling rate by tracking diminished returns. At each cooling step, modifications of the sequence are attempted in batches of 20,000. T is not reduced until a whole batch fails to find a better fit sequence. Cooling steps continue until 50 successive steps fail to generate a better fit. These two stopping values might need to be increased for larger data sets or those with more regional differences in sequence than we have encountered for Ordovician and Silurian graptolites.

The progress of an optimization may be watched via a screen graphic (Fig. 14B.8) that updates a misfit time series and animates a range chart or taxon richness curve with every trial. Thus CONOP enables users to recognize cooling schedules that are too fast (rapid initial fall in misfit comes to an abrupt halt) or too slow (falling misfit is continually interrupted by long batches of trials with no improvement in fitness). With a good cooling schedule the misfit curve approaches its minimum value smoothly and asymptotically. Rapid initial improvements in fitness give way to diminishing returns as the composite sequence is more finely tuned near the end of the search. On a good personal computer, data sets of the size described here may take almost a week to optimize.

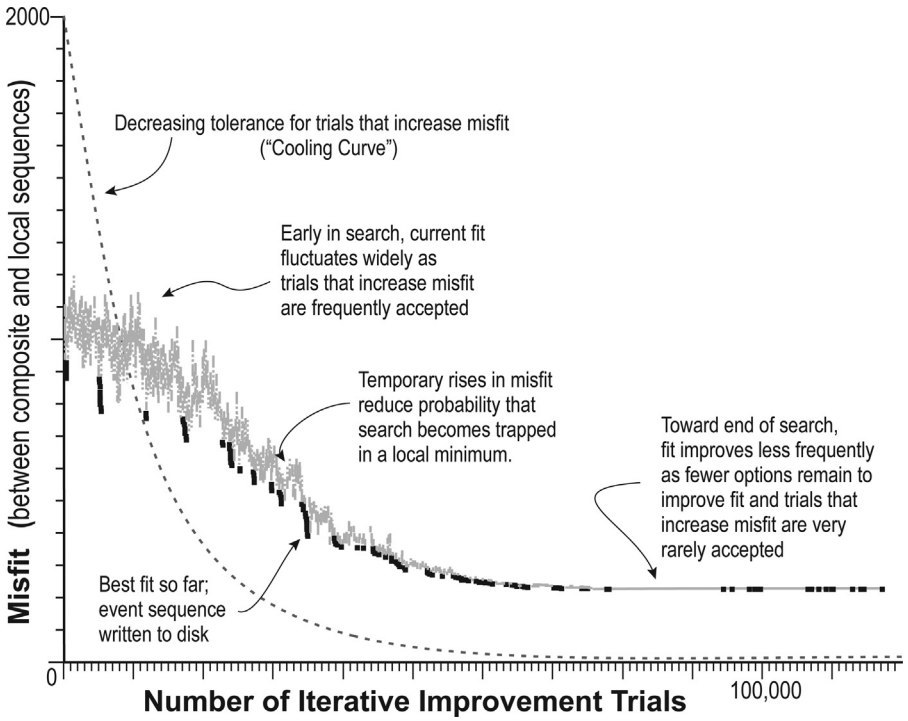

FIGURE 14B.8 Trajectory of generally improving fit (*black dots*) and diminishing returns during a simulated annealing search for the composite sequence that best fits a small problem set. The gray dots track accepted changes to the developing composite sequence; that is, all trials that reduce misfit and some that increase it. The acceptability of worsening fit decreases with the size of the deterioration and with time since the start of the search (*dashed line*).

14B.3 Projecting the composite sequence onto a time scale

The move from a composite sequence to a time scale proceeds in two steps. First, the spacing of events on the local thickness scales is used to generate a scaled composite section from the optimal global sequence. Second, a regression is chosen to interpolate an age scale between the dated events in the scaled composite section.

14B.3.1 From an ordinal to an interval composite sequence scale

Adjacent pairs of events in the optimized global sequence also have placements in the adjusted local sections (the inner optimization). These separations on local thickness scales may be combined in various ways to scale the separation of the events in the composite sequence (Sadler et al., 2009). Those pairs that are not placed at separate levels in any section, but always fall together, are now considered tied (zero spacing); they may contribute to evidence of mass extinction or bursts of origination. For the separable pairs a variety of averaging options is possible, but the "right" choice requires too much insight about variable rates of sediment accumulation and biotic turnover. Lacking adequate theoretical guidance, the practical choice is the one that simplifies the regression of the dated events. The consistently simplest option averages all the local spacing intervals for each pair of successive events, including zero values, after all sections have first been rescaled according to their relative span on the ordinal global sequence of events. The implicit assumption would be that biotic turnover tends to be more stable in the long term and large scale, while relative thickness is a better guide to relative duration in the short term and local scales (Sadler et al, 2009). There is no strong reason to believe that a smoother or more nearly linear disposition of dated tie points along the scaled composite sequence indicates more nearly true proxy time scale. It is preferred because it simplifies age interpolation.

14B.3.2 From a proxy interval scale to a time-scaled section

Agterberg et al. (Chapter 14A: Geomathematical and Statistical Procedures) discuss options available for interpolating age between dated events in the scaled composite section. The options differ in the complexity that the fitted curve is allowed to assume, but viable options must have nonnegative slope. Recall a similar consideration of options for the LOC. The search for the best fit LOC was an essentially ordinal step. Piecewise linear correlation was well suited to that exercise but is not the usual option of choice for timescaling. The preceding step that built the proxy time scale was already guided by a preference for smoothness in the distribution of dated events. By fitting the dated points in ensemble fashion, the global regression line does not necessarily pass through all dated calibration points. This may run counter to local expectations, where a very precise local age determination has been obtained from a bed very close to a stratigraphic unit boundary. The mismatch between regression and dated event may reach millions of years.

To explore this dilemma it is useful to examine locally weighted regression (LOWESS or its derivative LOESS), which can fit a curve with more or less complexity and approach something similar to piecewise linear correlation. Although LOWESS is often illustrated for broader and richer scatterplots, it is applicable to sparse and irregularly distributed data points such as arise during time scale calibration (Fig. 14B.9).

The spline technique, described in Chapter 14A, Geomathematical and Statistical Procedures, performs polynomial regressions between chosen data points or "knots." LOWESS (Cleveland, 1979, 1981; Cleveland and Devlin, 1988) performs a series of low-order (often linear) regressions within a sliding window that is focused (centered) on each calibration point in turn. The window captures a fixed number of points, the weights ω of which decrease with distance from the focal point. The weighting function is typically tricubic, with distance measured as a fraction of the maximum distance from the focal point. For points inside the sliding window, (dist/max dist ≤ 1),

$$\omega = \left(1 - \left(\frac{\text{dist}}{\text{max dist}}\right)^3\right)^3 \tag{14B.4}$$

Points beyond the window (dist/max dist > 1) are weighted zero.

Smaller windows enforce less smoothing, allowing the regression to more closely track "kinks" in the scatter plot of dated events. The smoothing factor α is usually chosen between 0.25 and 0.5. It expresses window size N_{loc} as the ratio of the number of points in the local regression window to the total number of calibration events N_{tot}.

$$\alpha = \frac{N_{\text{loc}}}{N_{\text{tot}}} \tag{14B.5}$$

The local regression equation is used to reposition the focal data point in each position of the sliding window. The repositioned values, when connected, form the LOESS curve. Similar to a weighted moving average, LOWESS curve fitting can proceed without first determining that a particular parametric form is appropriate. A corollary disadvantage is that no single equation is generated that estimates age for any level in the composite section. In effect, the regression slope is estimated at every point. Interpolations must be made by the LOWESS programs, which are available in R, for Excel and for other platforms.

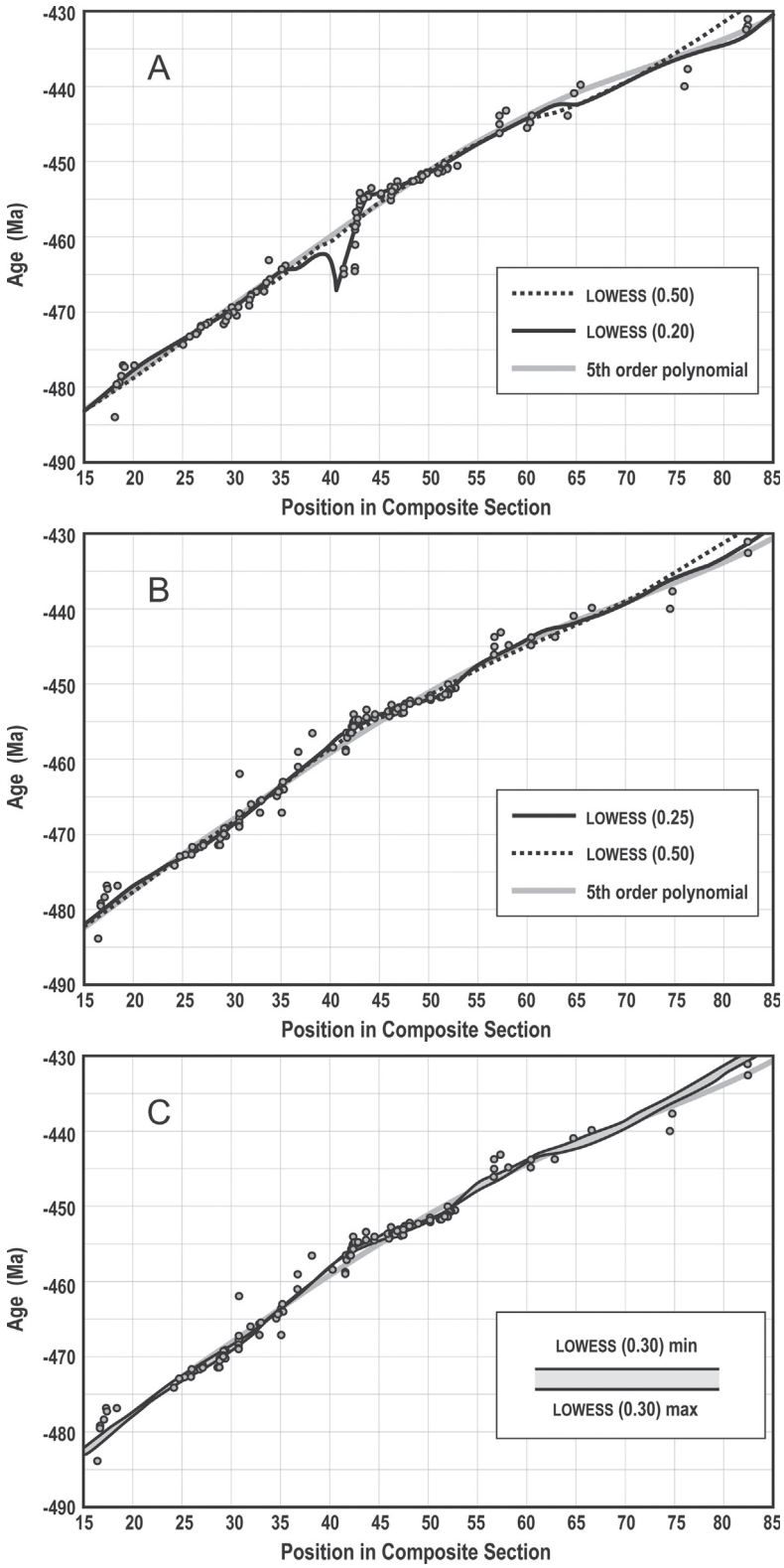

FIGURE 14B.9 Illustrative experiments with LOWESS regression of dated events entered as limits of uncertainty intervals (two circles per date): (A) regression (*black lines*) with limited smoothing (*solid line*) that overfits an anomaly in the distribution of dated events, which was caused by taxonomic error, and includes unacceptable negative slopes in portions of the regression; (B) improved fit with more smoothing, after taxonomic correction repositioned tie points in the global composite section; and (C) separate regressions for older and younger limits of uncertainty interval.

If the smoothing factor is too low, LOWESS regressions fit the data using locally negative slopes in the age calibration curves (Fig. 14B.9A). Eliminating such unreasonable slopes may determine the minimum degree of smoothing. More often, however, these anomalies help track down errors in the input data or their sequencing. Fig. 14B.9A was chosen to illustrate an extreme example of the impact of a taxonomic error on the array of Ordovician tie points. The anomaly was traced to its source and the taxonomy corrected (Fig. 14B.9B). In essence, every step in the time scale calibration exercise provides an opportunity for expert judgment to identify anomalies and exercise quality control on the input. This is possible because the composite sections bear resemblance to real stratigraphic sections, upon which biostratigraphic expertise is built. The LOESS regressions can develop confidence intervals. Fig. 14B.9C shows an experiment that used separate LOWESS regressions on the older and younger ends of the analytical uncertainty intervals.

The age calibration points for the Ordovician–Silurian time interval are unevenly distributed. None of the window sizes that are suited to the clusters of control points runs close to all calibration points where the data are relatively sparse. That is to say that a single smoothing factor does not fit all parts of a realistic Paleozoic calibration problem in which the stratigraphic spacing of dated events is highly uneven. Either window size would need to decrease as the stratigraphic separation of dated events increases or the weighting of the sparse regions would need to increase. Introducing too many ad hoc decisions reduces the objectivity of the interpolation in favor of expert judgment.

A common problem in regression is decreasing constraint near the ends of the data set. For LOESS regression this is clearly linked to a loss of points in the regression window. When time calibration is attempted for a single geologic period, it is unfortunate that the age regression weakens approaching the period boundaries. The advantage of placing geologic period calibrations together, as chapters in one volume, is the opportunity to perform age calibration exercises both within and across all chapters.

14B.3.3 Locating zone and stage boundaries

Ideally, expert stratigraphers approach the placement of biozone boundaries in a scaled composite just as they would in a real local section. In practice, however, the composite differs from real sections, perhaps because the compositing of so many local records is unlikely to be a perfect process, but more certainly because the composite has global scope that combines different local provinces and complex geographic ranges. Some anomalies in the composite section may be traced back to problems with the input data. Ordovician and Silurian composite sections revealed cases in which different stable isotope excursions appeared to have been given the same name. The immediate solution was to remove those data and rerun the optimization.

Composite taxon ranges may differ significantly in duration from local ranges (Fig. 14B.5). Experience has shown that index taxa tend to appear earlier in the composite sequence than expected. Since GTS2004 it has been recognized that zone boundaries may be better placed at the first appearance of a cluster of indicator taxa. Less commonly, a local index taxon is found to be relatively rare, globally, and does not meet a minimum number of local occurrences for robust placement in the composite sequence.

Global correlation of stage boundaries typically enjoys a more thorough and published effort than for zone boundaries. This presents three possible options for locating stage boundaries in a composite section. In the best reasoned option the boundary level is picked by an expert, familiar with the global discussion. For comparison, it can be instructive to include among the input records all published local placements of the boundary. They must be coded as local, shrink-to-fit uncertainty intervals, the size of which depends on the sampling intensity in the published section. In the emergent composite sequence the overlap of all the local uncertainties will be a consensus placement (e.g., Toarcian in Fig. 14B.1). One advantage of the published placements may be consideration of local ranges for fossil clades that were not included in the optimization process. A possible disadvantage might be the variety in vintage and quality of the local placements. Stage boundaries most often appear as sharp lines on published range charts; the data compiler is left to reconstruct a reasonable uncertainty based on the spacing of range ends.

A third option would use the definitive GSSP. By definition, this is a unique local event that does not adjust (a nail). Unfortunately, a unique local occurrence cannot be among the best constrained events for positioning in the composite sequence. Consider also the usual practice that establishes GSSPs at, or immediately below, the first occurrence of a taxon that is then used to estimate correlative horizons elsewhere. This places a nail at or below the older limit of a jack interval, which may be stretched downward in the global sequence to match evidence from other sections. A nail below a jack is not an immutable pairwise order. A more reliable local ordering, for correlation purpose, would pair the GSSP with a first appearance below it or a last appearance above. That is, recognizing that a GSSP lies within a taxon range zone or, better, within a coexistence interval would be more reliable and practical criteria for correlation. It might appear less precise but does represent a realistic uncertainly interval for time correlation. Finer resolving power could be achieved by increasing the number of concurrent taxon ranges that span the GSSP.

Stage and zone boundaries may be picked as uncertainty intervals. These uncertainties must be expected to expand when projected into the time scale across the confidence interval for the regression of dated calibration events.

14B.4 Slotting composite sections

Not only do expert zonal schemes differ by biotic province, they may also use different fossil clades. Ordovician and Silurian zones have been established for both graptolites and conodonts. Some dated events are best constrained by graptolite ranges, others by conodonts. Why not optimize data from both clades? Although nearly 2000 sections have been compiled that contain either conodonts or graptolites in this time interval, less than 150 of them record both clades in useful detail. If combined into one CONOP, events in the resulting composite sequence are unnaturally clustered by clade, because there is too little evidence of cross-clade coexistences.

Sadler and Cooper (2008) suggest how two separately optimized composite sequences might instead be slotted together, using constraints from those sections that yield taxa from both clades. Slotting algorithms (Clark, 1985; Gordon and Reyment, 1979; Thompson and Clark, 1993; and the more sophisticated dynamic programming variation, Lisiecki and Lisiecki, 2002) compare two sections, the samples of which form the rows and columns of a matrix. All pairs of samples are compared and a path of highest correlation is drawn, sample by sample across the matrix. With conodont and graptolite composite sequences as the rows and columns (Fig. 14B.10), Sadler and Cooper imagined identifying two off-diagonal areas of the matrix that the pathway could not enter without violating partial-ordering constraints derived from observations that a graptolite taxon FAD preceded a conodont LAD or a conodont FAD preceded a graptolite LAD in at least one of the local sections. The remaining cells would define a crudely diagonal channel for all feasible correlation pathways. Channel width would indicate the uncertainty of correlation. For the current graptolite and conodont composites, we find parts of the matrix where the pathway is occluded by overlap of the two out-of-bound regions (Fig. 14B.10). In other words the separate optimal composites for graptolites and conodonts are locally incompatible with sections that yield both clades. Assuming there are no taxonomic errors in the sections reporting both clades, one or both composites need adjustment.

One measure of the success of these time scale books is the extent to which they encourage researchers the most powerful new data. Clearly, progress for the older parts of the GTS problem places a premium on range charts from outcrops that yield two or more fossil clades, ideally with other events.

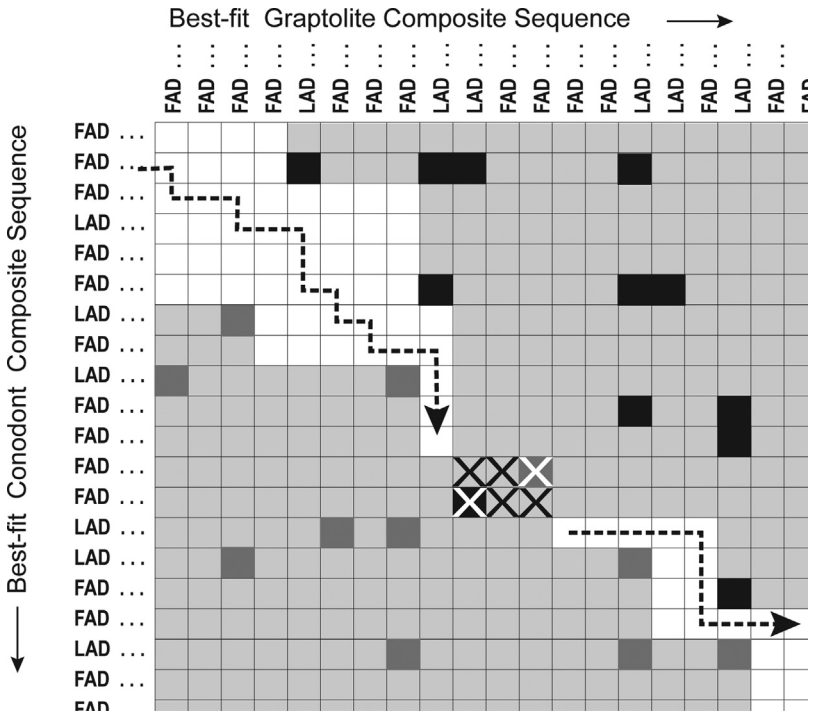

FIGURE 14B.10 Characteristics of slotting matrices that combine two composite sequences. Black cells: conodont FAD (First Appearance Datum) preserved below graptolite LAD (Last Appearance Datum). Dark gray cells: graptolite FAD preserved below conodont LAD. White cells: permissible pathways for line of correlation (LOC *dashed arrow*). Light gray cells: areas out of bounds to LOC. Crossed cells: occlusion of LOC pathway, indicating ordering error(s) in composite sequences. *LOC*, Line of correlation.

14B.5 Technical information

Technical information on the CONOP method and applications is in the website: https://drive.google.com/drive/folders/1xj5uZATaANSvhfauB-Je_YXsjSM468OH.

Bibliography

Agterberg, F.P., and Gradstein, F.M., 1999, The RASC method for ranking and scaling of biostratigraphic events. *Earth Science Reviews*, **46**: 1–25.

Agterberg, F.P., and Nel, L.D., 1982, Algorithms for the ranking of stratigraphic events. *Computers and Geoscience*, **8**: 69–90.

Alroy, J., 1992, Conjunction among taxonomic distributions and the Miocene mammalian biochronology of the Great Plains. *Paleobiology*, **18**: 326–343.

Alroy, J., 1994, Appearance event ordination: a new biochronologic method. *Paleobiology*, **20**: 191–207.

Berry, W.B.N., 1968, *Growth of a Prehistoric Time Scale Based on Organic Evolution*. San Francisco, CA: W. H. Freeman, p. 158.

Clark, R.M., 1985, A FORTRAN program for constrained sequence-slotting based on minimum combined path length. *Computers and Geoscience*, **11**: 605–617.

Cleveland, W.S., 1979, Robust locally weighted regression and smoothing scatterplots. *Journal of the American Statistical Association*, **74**: 829–836.

Cleveland, W.S., 1981, LOWESS: a program for smoothing scatter plots by robust locally weighted regression. *The American Statistician*, **35**: 54, https://doi.org/10.2307/268359.

Cleveland, W.S., and Devlin, S.J., 1988, Locally weighted regression: an approach to regression analysis by local fitting. *Journal of the American Statistical Association*, **83**: 596–610.

Cody, R.D., Levy, R.H., Harwood, D.M., and Sadler, P.M., 2008, Thinking outside the zone: high-resolution quantitative diatom biochronology for the Antarctic Neogene. *Palaeogeography, Paleoclimatology, Palaeoecology*, **260**: 92–121.

Cooper, R.A., Crampton, J.S., Raine, J.I., Gradstein, F.M., Morgans, H. E.G., Sadler, P.M., et al., 2001, Quantitative biostratigraphy of the Taranaki Basin, New Zealand: a deterministic and probabilistic approach. *American Association of Petroleum Geologists Bulletin*, **85**: 1469–1498.

Cooper, R.A., and Lindholm, K., 1990, A precise worldwide correlation of early Ordovician graptolite sequences. *Geological Magazine*, **127**: 497–525.

Daneshian, J., Ramezani Dana, L., and Sadler, P.M., 2017, A composite foraminiferal biostratigraphic sequence for the Lower Miocene deposits in the type area of the Qom Formation, central Iran, developed by constrained optimization (CONOP). *Journal of African Earth Sciences*, **125**: 214–229.

Dell, R.F., Kemple, W.G., and Tovey, C.A., 1992, Heuristically solving the stratigraphic correlation problem. *In Proceedings of the First Industrial Engineering Research Conference*, Vol. 1, pp. 293–297.

Edwards, L.E., 1978, Range charts and no-space graphs. *Computers and Geoscience*, **4**: 247–255.

Fan, J., and Zhang, Y.D., 2000, Sinocor 1.0, a biostratigraphic program for graphic correlation. *Acta Palaeontologica Sinica*, **39**: 573–583.

Glazner, A.F., and Sadler, P.M., 2016, Estimating the duration of geologic intervals from a small number of age determinations: a challenge common to petrology and paleobiology. *Geochemistry, Geophysics, Geosystems*, **17**: 4892–4898, https://doi.org/10.1002/2016GC006542.

Gordon, A.D., and Reyment, R.A., 1979, Slotting of borehole sequences. *Mathematical Geology*, **11**: 309–327.

Gradstein, F., Ogg, J.G., and Smith, A.G., 2004, *A Geological Time Scale*. Cambridge University Press, p. 589.

Grubb, B.J., and Finney, S.C., 1995, Graphic correlation of Middle Ordovician graptolite-rich shales, southern Appalachians: successful application of a technique to inadequate stratigraphic sections. *In* Mann, K.O., and Lane, H.R. (eds), Graphic Correlation. *SEPM Special Publication,* **53**: 151–158.

Guex, J., 1977, Une nouvelle méthode d'analyse biochronologique. *Bulletin Laboratoire Géologique Lausanne*, **224**: 309–322.

Guex, J., 1991, *Biochronological Correlations*. Berlin: Springer Verlag, p. 250.

Hints, O., Nõlvak, J., Paluveer, L., and Tammekänd, M., 2011, Conventional and CONOP9 approaches to biodiversity of Baltic Ordovician chitinozoans. *Cuadernos del Museo Geominero del Instituto Geológico y Minero de España*, **14**: 243–249.

Hood, K.C., 1986, *Graphcor – Interactive Graphic Correlation*, version 2.2: copyright K. C, Hood.

Kaufmann, B., 2006, Calibrating the Devonian time scale: a synthesis of U-Pb-TIMS ages and conodont stratigraphy. *Earth Science Reviews*, **76**: 175–190, https://doi.org/10.1016/j.earscirev.2006.01.001.

Kemple, W.G., Sadler, P.M., and Strauss, D.J., 1989, A prototype constrained optimisation solution to the time correlation problem. *In* Agterberg, F.P., and Bonham-Carter, G.F. (eds), *Statistical Applications in the Earth Sciences*. Ottawa, ON: Geological Survey of Canada Paper, 417–425.

Kemple, W.G., Sadler, P.M., and Strauss, D.J., 1995, Extending graphic correlation to many dimensions: stratigraphic correlation as constrained optimization. *In* Mann, K.O., and Lane, H.R. (eds), Graphic Correlation. *SEPM Special Publication,* **53**: 65–82.

Kirkpatrick, S., Gelatt, C.D., and Vecchi, M.P., 1983, Optimization by simulated annealing. *Science*, **220**: 671–680, https://doi.org/10.1126/science.220.4598.671.

Kleffner, M.A., and Barrick, J.E., 2011, Telychian – early Sheinwoodian (Early Silurian) conodont-, graptolite-, chitinozoan- and event-based chronostratigraphy developed using the graphic correlation method. *Memoirs of the Association of Australasian Palaeontologists*, **39**: 191–210.

Lisiecki, L.E., and Lisiecki, P.A., 2002, Application if dynamic programming to the correlation of paleoclimate records. *Paleoceanography*, **17**: 12, https://doi.org/10.1029/2001PA000733.

MacLeod, N., and Sadler, P.M., 1995, Estimating the line of correlation. *In* Mann, K.O., and Lane, H.R. (eds), Graphic Correlation. *SEPM Special Publication,* **53**: 51–64.

Mann, K.O., and Lane, H.R., 1995, Graphic correlation: a powerful stratigraphic technique comes of age. *In* Mann, K.O., and Lane, H.R. (eds), Graphic Correlation. *SEPM Special Publication,* **53**: 3–13.

Marshall, C.R., 2010, Using confidence intervals to quantify the uncertainty in the end points of stratigraphic ranges. *In* Alroy, J., and Hunt, G. (eds), *The Paleontological Society Papers* **16**: 291–316.

Monnet, C., Klug, C., Goudemand, N., De Baets, K., and Bucher, H., 2011, Quantitative biochronology of Devonian ammonoids from Morocco and proposals for a refined unitary association method. *Lethaia*, **44**: 469–489.

Riedman, L.A., and Sadler, P.M., 2018, Global species richness and biostratigraphic potential of early to middle Neoproterozoic eukaryote

fossils. *Precambrian Research*, **319**: 6–18, https://doi.org/10.1016/j.precamres.2017.10.008.

Rubel, M., Nestor, V., Harris, M.T., Sheehan, P.M., Ainsaar, L., Männik, P., et al., 2006, A new high-resolution chitinozoan composite standard for the East Baltic Lower Silurian succession based on numerical analysis. *Geological Quarterly*, **50**: 323–332.

Sadler, P.M., 1981, Sediment accumulation rates and the completeness of stratigraphic sections. *Journal of Geology*, **89**: 569–584.

Sadler, P.M., 2004, Quantitative biostratigraphy – achieving finer resolution in Global Correlation. *Annual Reviews of Earth and Planetary Sciences*, **32**: 187–213.

Sadler, P.M., 2006, Composite time lines: a means to leverage resolving power from radioisotopic dates and biostratigraphy. *In* Olszewski, T. (ed), Geochronology: Emerging Opportunities. *Paleontological Society Papers,* **12**: 145–170.

Sadler, P.M., 2010, Brute-force biochronology: sequencing paleobiologic first- and last-appearance events by trial and error. *In* Alroy, J., and Hunt, G. (eds), Quantitative Methods in Paleobiology. *Paleontological Society Papers,* **16**: 271–289.

Sadler, P.M., 2012, Integrating carbon isotope excursions into automated stratigraphic correlations: an example from the Silurian of Baltica. *Bulletin of Geosciences*, **84**: 681–694, https://doi.org/10.3140/bull.geosci.1307.

Sadler, P.M., and Cervato, C., 2011, Data and tools for geologic timelines and timescales. *In* Keller, G.R., and Baru, C. (eds), *Geoinformatics*. Cambridge University Press, 145–165.

Sadler, P.M., and Cooper, R.A., 2008, Improved resolution and quantified stratigraphic uncertainty – time scales of the future. *Newsletters on Stratigraphy*, **43**: 49–53, https://doi.org/10.1127/0078-0421/2008/0043-0049.

Sadler, P.M., Kemple, W.G., and Kooser, M.A., 2003, CONOP9 programs for solving the stratigraphic correlation and seriation problems as constrained optimization. *In* Harries, P.J. (ed), High-Resolution Approaches in Stratigraphic Paleontology. Topics in Geobiology. *Dordrecht: Kluwer Academic Publishers,* **21**: 461–465.

Sadler, P.M., Cooper, R.A., and Melchin, M.J., 2009, High-resolution, early Paleozoic (Ordovician-Silurian) time scales. *Geological Society of America Bulletin*, **121**: 887–906.

Sadler, P.M., Cooper, R.A., and Melchin, M.J., 2011, Sequencing the graptoloid clade: building a global diversity curve from local range charts, regional composites and global time-lines. *Proceedings of the Yorkshire Geological Society*, **58**: 329–343.

Sadler, P.M., Cooper, R.A., and Crampton, J.S., 2014, High-resolution geobiologic time lines: progress and potential, fifty years after the advent of graphic correlation. *The Sedimentary Record*, **12**: 4–9, https://doi.org/10.2110/sedred.2014.3.

Sadler, P.M., and Sabado, J.A., 2009, Automated correlation, seriation, and the treatment of biotic dissimilarity. *Museum of Northern Arizona Bulletin*, **65**: 21–35.

Savary, J., and Guex, J., 1991, Biograph: un nouveau programme de consruction des correlations biochronologique basées sur les associations unitaires. *Bulletin Laboratoire Géologique Lausanne*, **313**: 317–340.

Shaw, A.B., 1964, *Time in Stratigraphy*. New York: McGraw-Hill, p. 365.

Shaw, A.B., 1995, Early history of graphic correlation. *In* Mann, K.O., and Lane, H.R. (eds), Graphic Correlation. *SEPM Special Publication,* **53**: 15–19.

Shen, S.Z., Crowley, J.L., Wang, Y., Bowring, S.A., Erwin, D.H., Sadler, P.M., et al., 2011, Calibrating the End-Permian mass extinction. *Science*, **334**: 1367–1372.

Strauss, D.J., and Sadler, P.M., 1989, Classical confidence intervals and the Bayesian probability estimates for ends of local taxon ranges. *Mathematical Geology*, **21**: 411–427.

Sweet, W.C., 1984, Graphic correlation of upper Middle and Upper Ordovician rocks, North American Midcontinental Province, USA. *In* Bruton, D.L. (ed), Aspects of the Ordovician System. *Paleontological Contributions of the University of Oslo,* **295**: 23–25.

Sweet, W.C., 1995, Graphic assembly of a conodont-based composite standard for the Ordovician system of North America. *In* Mann, K.O., and Lane, H.R. (eds), Graphic Correlation. *SEPM Special Publication,* **53**: 139–150.

Sweet, W.C., 2005, Graphical refinement of the conodont database: examples and a plea. *Palaeontology*, **73**: 135–141.

Thompson, R., and Clark, R.M., 1993, Quantitative marine sediment core matching using a modified sequence-slotting algorithm. *In* Hailwood, E.A., and Kidd, R.B. (eds), *High Resolution Stratigraphy*. London: Geological Society of London, 39–49.

Tipper, J.C., 1988, Techniques for quantitative stratigraphic correlations: a review and annotated bibliography. *Geological Magazine*, **125**: 475–494.

Webster, M., Sadler, P.M., Kooser, M.A., and Fowler, E., 2003, Combining stratigraphic sections and museum collections to increase biostratigraphic resolution. *In* Harries, P.J. (ed), *High Resolution Approaches in Stratigraphic Paleontology*. Dordrecht: Kluwer Academic Publishers, 95–128.